Cell Reports

Article

FANCM promotes PARP inhibitor resistance by minimizing ssDNA gap formation and counteracting resection inhibition

Graphical abstract

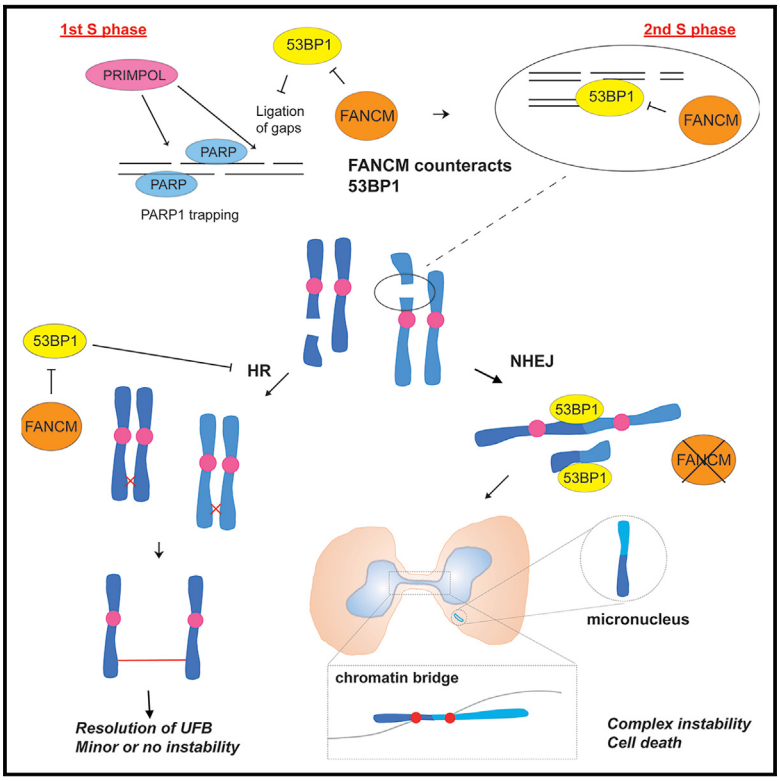

Highlights

- Cells depleted of FANCM exhibit increased sensitivity to PARP inhibitors
- FANCM depletion leads to elevated ssDNA gap formation behind replication forks
- Reduced end resection of collapsed forks is observed in FANCM-deficient cells
- FANCM counteracts 53BP1 to repair PARP inhibitor-induced DNA damage

Authors

Zeyuan Liu, Huadong Jiang, Sze Yuen Lee, Nannan Kong, Ying Wai Chan

Correspondence

gywchan@hku.hk

In brief

Liu et al. reveal FANCM's role in promoting PARP inhibitor resistance, independent of the core Fanconi anemia complex, by counteracting 53BP1. FANCM depletion results in increased DNA damage, elevated ssDNA gap formation, and reduced resection of collapsed forks, leading to extensive cell death, highlighting its significance in PARP inhibitor response.

Liu et al., 2024, Cell Reports *43*, 114464
July 23, 2024
https://doi.org/10.1016/j.celrep.2024.114464

CellPress

Cell Reports

CellPress
OPEN ACCESS

Article

FANCM promotes PARP inhibitor resistance by minimizing ssDNA gap formation and counteracting resection inhibition

Zeyuan Liu,[1] Huadong Jiang,[1] Sze Yuen Lee,[1] Nannan Kong,[1] and Ying Wai Chan[1,2,*]
[1]School of Biological Sciences, The University of Hong Kong, Pokfulam, Hong Kong SAR, China
[2]Lead contact
*Correspondence: gywchan@hku.hk
https://doi.org/10.1016/j.celrep.2024.114464

SUMMARY

Poly(ADP-ribose) polymerase inhibitors (PARPis) exhibit remarkable anticancer activity in tumors with homologous recombination (HR) gene mutations. However, the role of other DNA repair proteins in PARPi-induced lethality remains elusive. Here, we reveal that FANCM promotes PARPi resistance independent of the core Fanconi anemia (FA) complex. FANCM-depleted cells retain HR proficiency, acting independently of BRCA1 in response to PARPis. FANCM depletion leads to increased DNA damage in the second S phase after PARPi exposure, driven by elevated single-strand DNA (ssDNA) gap formation behind replication forks in the first S phase. These gaps arise from both 53BP1- and primase and DNA directed polymerase (PRIMPOL)-dependent mechanisms. Notably, FANCM-depleted cells also exhibit reduced resection of collapsed forks, while 53BP1 deletion restores resection and mitigates PARPi sensitivity. Our results suggest that FANCM counteracts 53BP1 to repair PARPi-induced DNA damage. Furthermore, FANCM depletion leads to increased chromatin bridges and micronuclei formation after PARPi treatment, elucidating the mechanism underlying extensive cell death in FANCM-depleted cells.

INTRODUCTION

In 2005, a groundbreaking discovery revealed that inhibiting poly(ADP-ribose) polymerase (PARP) triggers significant cell death in cancer cells deficient in either *BRCA1* or *BRCA2*.[1,2] These proteins play a critical role in repairing double-stranded breaks (DSBs) through homologous recombination (HR).[3] Tumors harboring mutations in other HR genes are often referred to as having "BRCAness" and share similar therapeutic vulnerabilities with BRCA-mutated tumors.[4] For instance, cells deficient in other HR genes, such as ATM, ATR, PALB2, RAD51C, RAD51D, and MUS81, are hypersensitive to PARP inhibitors (PARPis).[4–8] Currently, four PARPis—olaparib, niraparib, rucaparib, and talazoparib—have received FDA approval.[9] PARPis have demonstrated remarkable clinical success in treating breast, ovarian, prostate, and pancreatic cancers, particularly in patients carrying germline mutations in *BRCA1/2*. However, the efficacy of PARPis in non-*BRCA*-mutated tumors remains uncertain.

Several models have been proposed to elucidate how PARPi selectively targets HR-deficient cells. One such model proposes that DSBs might be the primary sensitizing lesion. As PARP plays a crucial role in single-strand break (SSB) repair, its inhibition leads to an increase in SSBs, which are then converted to DSBs upon encountering replication forks during the S phase.[1,2,10] In BRCA-deficient cells, DSBs cannot be properly repaired, resulting in hypersensitivity to PARPis. Moreover, BRCA1 and BRCA2 protect stalled replication forks from nucleolytic degradation.[11–13] PARPis can trap PARP1 (the most abundant PARP protein) on DNA, interfering with DNA replication and promoting fork collapse and degradation in BRCA-mutated cells.[14,15] Interestingly, PARPis have been shown to accelerate fork progression,[16] likely because PARP1 facilitates fork reversal, an important mechanism for decelerating or pausing the progression of replication forks.[17–20] Consequently, PARPis lead to unrestrained replication and more frequent DSB formation.

Recently, several studies have proposed that ssDNA gaps induced by PARPis, rather than DSBs, may be the primary cause of toxicity in BRCA-deficient cells.[21–23] PARPis induce ssDNA gaps in both lagging and leading strands behind replication forks. As a sensor of unligated Okazaki fragments, PARP1 facilitates their repair, preventing the accumulation of ssDNA gaps in lagging strands.[24,25] Additionally, PARP inhibition either through olaparib treatment[26,27] or loss of CARM1, a PARP-stimulating factor,[28] increases PRIMPOL (primase and DNA directed polymerase)-mediated repriming of stalled forks, resulting in the formation of ssDNA gaps in leading strands. These ssDNA gaps behind replication forks can persist into the second S phase, leading to fork collapse and DSB formation.[29] Furthermore, ssDNA-containing replication intermediates can be transmitted into mitosis, inducing mitotic defects in BRCA-deficient cells, ultimately causing genome instability and cell death.[22,30–32]

Despite significant clinical success in treating patients with *BRCA*-mutated cancer, both *de novo* and acquired resistance to PARPis are observed. In clinical settings, re-expression or

reversion mutations of *BRCA1/2* have been observed to restore HR activity and result in PARPi resistance in patients harboring BRCA2 mutations.[33–38] Moreover, secondary mutations in RAD51C and RAD51D that increase HR have been identified in patients treated with rucaparib.[39] Several other mechanisms causing PARPi resistance have also been discovered through laboratory research. Firstly, a reduction in PARP1 trapping, caused by PARP1 depletion, mutations in the DNA-binding domain of PARP1, or loss of PAR glycohydrolase, leads to PARPi resistance.[15,40,41] Secondly, in *BRCA1*-mutated cells, HR activity can also be restored by mutations that reduce resection inhibition. The loss of any component of the 53BP1-RIF1-REV7-Shieldin pathway rescues DNA end resection, rendering cells resistant to PARPis.[42–50] Other factors downstream of 53BP1, such as the CTC1-STN1-TEN1 complex[51,52] and DYNLL1,[53,54] have been reported to antagonize resection, and their loss also results in PARPi resistance. Thirdly, stalled forks are unprotected in the absence of BRCA1/2, leading nucleases like MUS81 and MRE11 to attack stalled forks, degrade nascent strand DNA, and induce fork collapse. Depletion of proteins that promote MRE11/MUS81 recruitment to stalled forks—such as PTIP, CHD4, and EZH2—results in fork protection and PARPi resistance.[55–57] Fourthly, loss of folk remodelers, such as SMARCAL1, has been shown to promote PARPi resistance in BRCA-deficient cells,[58] likely because SMARCAL1-induced reversed forks can be degraded by MRE11. Fifthly, DNA polymerase θ overexpression is observed in some HR-defective tumors.[59,60] This overexpression leads to the upregulation of microhomology-mediated end joining and postreplicative ssDNA gap filling,[23] thus promoting PARPi resistance. Finally, the upregulation of drug efflux by overexpressing ABCB1 induces PARPi resistance.[61,62]

FANCM is one of the Fanconi anemia (FA) genes that play a critical role in repairing DNA interstrand crosslinks.[63] FANCM also contributes to genome stability through FA-independent mechanisms. For example, FANCM's translocase activity modulates stalled replication forks, promoting their recovery.[64–66] FANCM interacts with FAAP24 to activate the ATR/CHK1 checkpoint[67,68] and with the BLM (Bloom syndrome protein)-TOP3A-RMI1-RMI2 complex to suppress sister chromatid exchange, long-tract gene conversion, and tandem duplication at stalled forks.[69,70] Furthermore, the FANCM-MHF1/2 complex mediates the replication traverse of an interstrand DNA crosslink,[71,72] and FANCM collaborates with BLM to suppress alternative lengthening of telomeres.[73–75] Patient-derived *FANCM*$^{-/-}$ cell lines were shown to be hypersensitive to PARPis,[76,77] but the underlying mechanism remains unclear. In this study, we investigated how FANCM promotes PARPi resistance. We found that FANCM-depleted cells exhibit increased ssDNA gaps behind replication forks, leading to a surge of DNA damage in the second S phase. These cells also display reduced end resection of collapsed forks. Therefore, FANCM plays a dual role in the first and second S phases upon PARPi exposure.

RESULTS

FANCM promotes PARPi resistance independent of the FA core complex

We aim to study how FANCM promotes PARPi resistance. To examine the immediate effects of FANCM depletion, we employed an auxin-inducible degron method to facilitate rapid degradation[78,79] (Figure 1A). We engineered HCT116 cells with endogenous FANCM C-terminally tagged with a mini-auxin-inducible degron (mAID) and a GFP using CRISPR-Cas9 technology. Moreover, these cells express an F box protein, OsTIR1, upon the addition of doxycycline (Dox). This allows for the degradation of mAID-tagged proteins when treated with auxin (indole-3-acetic acid, IAA). Treatment with Dox and IAA for 48 h induced a near-complete depletion of FANCM (Figure 1B). The expression of OsTIR1 is the limiting factor for the degradation, as pre-treating HCT116$^{FANCM\text{-}mAID\text{-}GFP}$ cells with Dox for 48 h and further addition of IAA for 6 h were sufficient to induce a clear depletion of FANCM (Figure S1A). We performed PCR of the purified genomic DNA to confirm that both alleles of *FANCM* were tagged (Figures 1A and S1B). Since successful tagging disrupted p2 priming, biallelic tagging led to only a ~1,000 bp product with primers p1 and p3, while monoallelic tagging led to a ~1,000 bp product and a ~200 bp product with primers p1 and p2 (Figure S1B). To test if depletion of FANCM affects the drug sensitivity of cells, we treated HCT116$^{FANCM\text{-}mAID\text{-}GFP}$ cells with a panel of DNA damaging agents, including cisplatin, hydroxyurea (HU), camptothecin (CPT), methyl methanesulfonate (MMS), etoposide, and two PARPis, olaparib and veliparib, and measured their long-term survival by clonogenic assays (Figures 1C–1E and S1C–S1F). FANCM depletion (+Dox, IAA) induced hypersensitivity to cisplatin, CPT, MMS, and etoposide but not to HU, as previously reported (Figures 1C and S1C–S1F).[64,65,69,80,81] Importantly, cells depleted of FANCM were hypersensitive to both olaparib and veliparib (Figures 1D and 1E). As a control, we also tested HCT116^{TIR1} cells. Treatment with Dox and IAA did not induce any drug sensitivity in HCT116^{TIR1} cells (Figures S1G–S1L).

Next, we investigated whether promoting PARPi resistance is an FA-independent function of FANCM. Cells were depleted with FANCM or FANCB (a core component of the FA complex) using small interfering RNAs (siRNAs). Depletion of either FANCM or FANCB abolished the chromatin association of FANCD2, indicating their efficient depletion (Figure 1F). Importantly, while both FANCM- or FANCB-depleted cells were sensitive to cisplatin, only FANCM-depleted cells displayed sensitivity to PARPis (Figures 1G–1I). These results indicate that the role of FANCM in promoting PARPi resistance is independent of the FA core complex.

FANCM depletion does not impair HR, and it acts independently of BRCA1

One possible explanation of why FANCM depletion induces PARPi sensitivity is that FANCM is required for efficient HR. To test this, 239 cells with a DR-GFP reporter were employed to measure HR-mediated DSB repair (Figure 2A). The reporter cassette contains a mutant GFP (SceGFP) with an I-SceI site. Transfection of the I-SceI restriction enzyme induces DSBs, which can be repaired by HR using an iGFP fragment as the template for nascent DNA synthesis, resulting in the restoration of a functional GFP.[82] DR-GFP cells were transfected with control, BRCA1, or FANCM siRNAs, together with plasmids expressing RFP (as a transfection marker) and I-SceI. The efficiency of BRCA1 depletion is verified by the reduction of

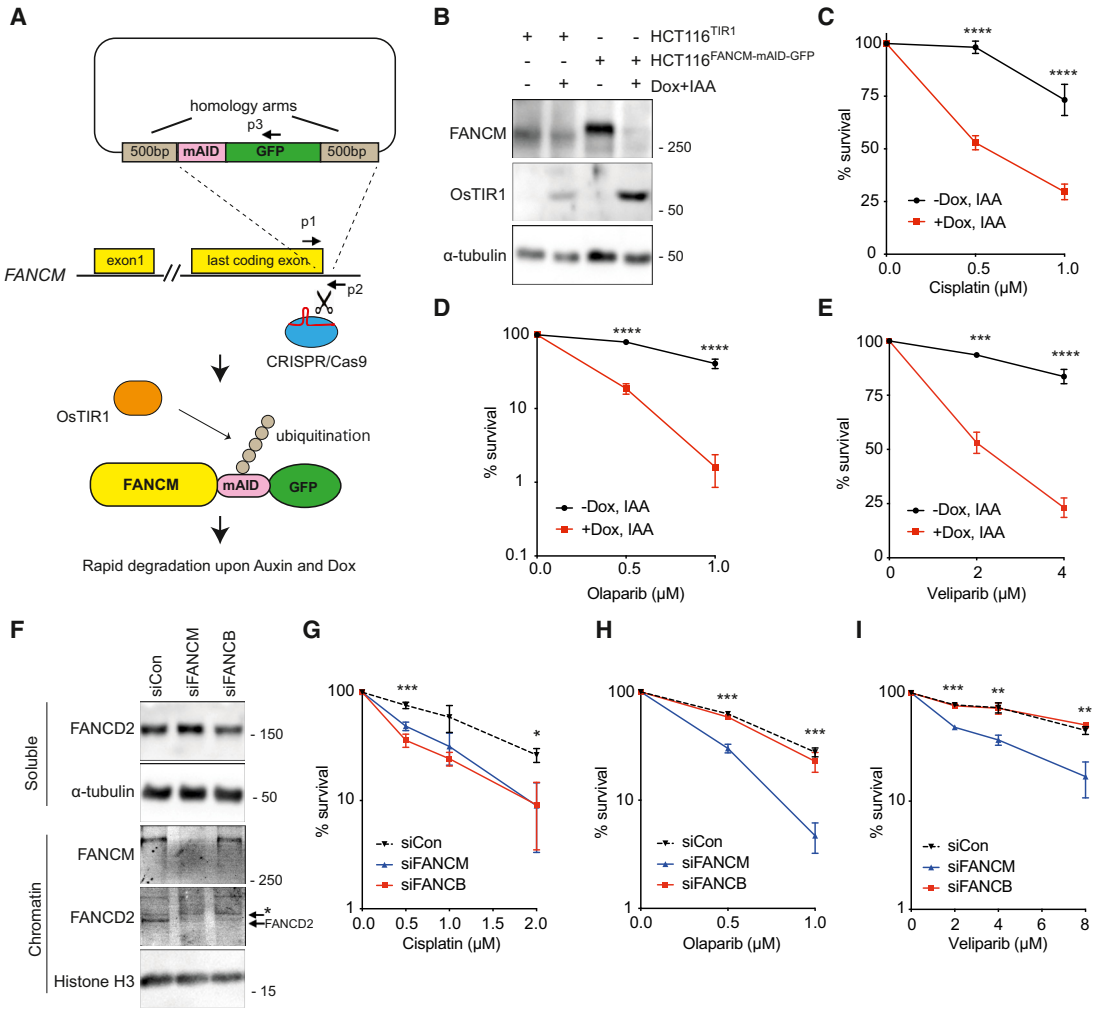

Figure 1. Depletion of FANCM, but not FANCB, induces hypersensitivity to PARPis

(A) Schematic diagram of the construction of an HCT116 cell line with FANCM C-terminally tagged with a mAID and a GFP. Positions of primers p1, p2, and p3 designed to confirm bi-allelic tagging are shown.

(B) Cells were treated with Dox and IAA for 48 h. Depletion of FANCM was verified by western blotting.

(C–E) Clonogenic cell survival assays were carried out on HCT116$^{FANCM\text{-}mAID\text{-}GFP}$ cells treated with or without Dox and IAA and the indicated concentrations of cisplatin, olaparib, and veliparib.

(F) Cells depleted of FANCM or FANCB by siRNAs were fractionated to separate soluble and chromatin fractions. The fractions were analyzed by western blotting for the indicated proteins.

(G–I) Clonogenic cell survival assays were carried out on mock-depleted, FANCM-depleted, and FANCB-depleted cells. They were treated with indicated concentrations of cisplatin, olaparib, and veliparib.

Data in (C)–(E) and (G)–(I) are represented as mean ± SD, $n = 3$ independent experiments. p values were determined using an unpaired two-tailed t test.

See also Figure S1.

immunofluorescent staining of BRCA1 (Figure S2A). As expected, depletion of BRCA1 significantly reduced the level of HR repair compared with mock-depleted cells, as indicated by the significant reduction of GFP-positive cells (Figures 2B and 2C). Importantly, cells depleted of FANCM displayed a similar level of HR repair to that of mock-depleted cells, indicating that FANCM-depleted cells are proficient in repairing DSBs by HR.

Next, we investigated the genetic relationship between BRCA1 and FANCM. Depletion of FANCM (+Dox, IAA) and depletion of BRCA1 (by siRNA) in HCT116$^{FANCM\text{-}mAID\text{-}GFP}$ cells showed a similar increase in sensitivity to olaparib and veliparib (Figures 2D and 2E). Importantly, co-depletion of FANCM and BRCA1 induced a further increase in sensitivity to both PARPis. These results suggest that FANCM acts independently of BRCA1 in response to PARP inhibition. We further confirmed the effect of FANCM depletion in two breast cancer cell lines, MCF-7 (which expresses wild-type BRCA1) and SUM149PT (which expresses a truncated mutant of BRCA1). Depletion of FANCM by two independent siRNAs induced a clear increase in sensitivity to olaparib in both cell lines (Figures S2B–S2E).

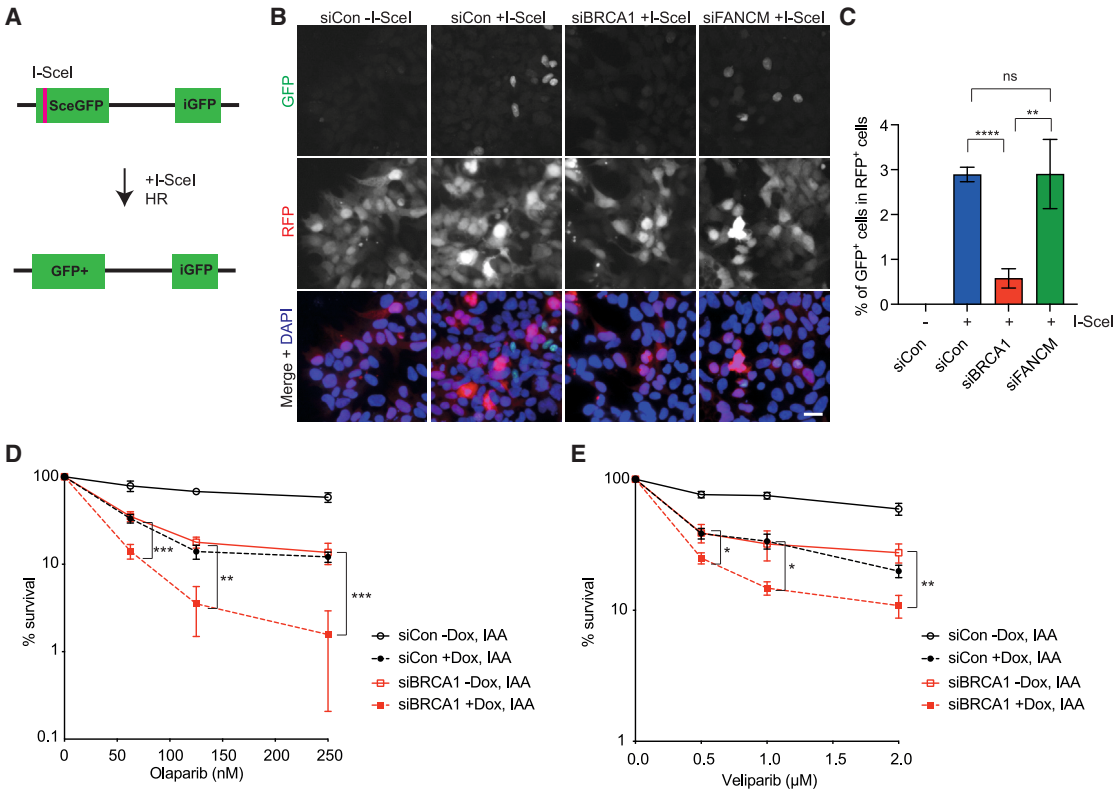

Figure 2. FANCM-depleted cells are HR proficient

(A) Schematic diagram of the DR-GFP reporter. I-SceI induces a DSB, and HR uses iGFP as the repair template, resulting in the restoration of a GFP.

(B) 293 DR-GFP cells were treated with control, FANCM, or BRCA1 siRNAs together with or without the I-SceI-expressing plasmids. They were all co-transfected with RFP-expressing plasmids. Scale bar, 10 μm.

(C) Quantification of GFP-positive cells in RFP-positive cells.

(D and E) Clonogenic cell survival assays were carried out on HCT116$^{FANCM\text{-}mAID\text{-}GFP}$ cells (±Dox, IAA) treated with control or BRCA1 siRNAs. They were then treated with indicated concentrations of olaparib and veliparib.

Data in (C) are represented as mean ± SD, $n = 4$ independent experiments. Data in (D) and (E) are represented as mean ± SD, $n = 3$ independent experiments. p values were determined using an unpaired two-tailed t test.

See also Figure S2.

FANCM depletion induces an increased DDR in the second S phase

Since PARP inhibition induces DNA damage mainly in the S phase, we monitored the cell cycle progression of S phase cells upon olaparib treatment using an EdU pulse-chase experiment. We briefly exposed mock-depleted or FANCM-depleted cells to EdU (30 min) to pulse label S phase cells (EdU$^+$). Following olaparib treatment, cells were collected for DNA content analysis at different time points (Figure 3A), allowing us to track the progression of EdU$^+$ cells through the cell cycle during olaparib treatment. From t = 0 to 8 h, EdU$^+$ cells advanced to G2 and the subsequent G1 phase. By t = 24 h, most cells had entered the second S phase. At t = 32 to 48 h, both mock-depleted and FANCM-depleted cells were primarily arrested in the second G2 phase (Figure 3A). These results align with previous findings that DSBs form when ssDNA gaps, induced by PARPis, convert to DSBs due to replication fork collapse in the second S phase, leading to cell-cycle arrest in the second G2 phase.[29]

To determine whether PARPis induce more DNA damage and stronger activation of the DNA damage response (DDR) in FANCM-depleted cells, we treated HCT116$^{FANCM\text{-}mAID\text{-}GFP}$ cells (±Dox, IAA) with olaparib and collected cells at different time points (0–48 h, Figure 3B). In both mock-depleted and FANCM-depleted cells, the levels of phosphorylated CHK1 (CHK1-pS317) increased from the early time point (t = 8 h), consistent with PARPi-induced fork stalling. Mock-depleted cells exhibited a noticeable increase in phosphorylation of replication protein A2 (RPA2-pS4/S8) and CHK2 (CHK2-pT68) primarily at later time points (t = 24 to 48 h), suggesting that DSBs are mainly induced in the second S phase (Figure 3B). Notably, FANCM-depleted cells displayed higher levels of CHK2-pT68 than mock-depleted cells, indicating increased DNA damage (Figure 3B, lanes 4–5 vs. lanes 9–10). Surprisingly, the level of RPA2-pS4/S8 in FANCM-depleted cells at t = 24 to 48 h was lower compared to that of mock-depleted cells, suggesting reduced ssDNA formation in the second S phase.

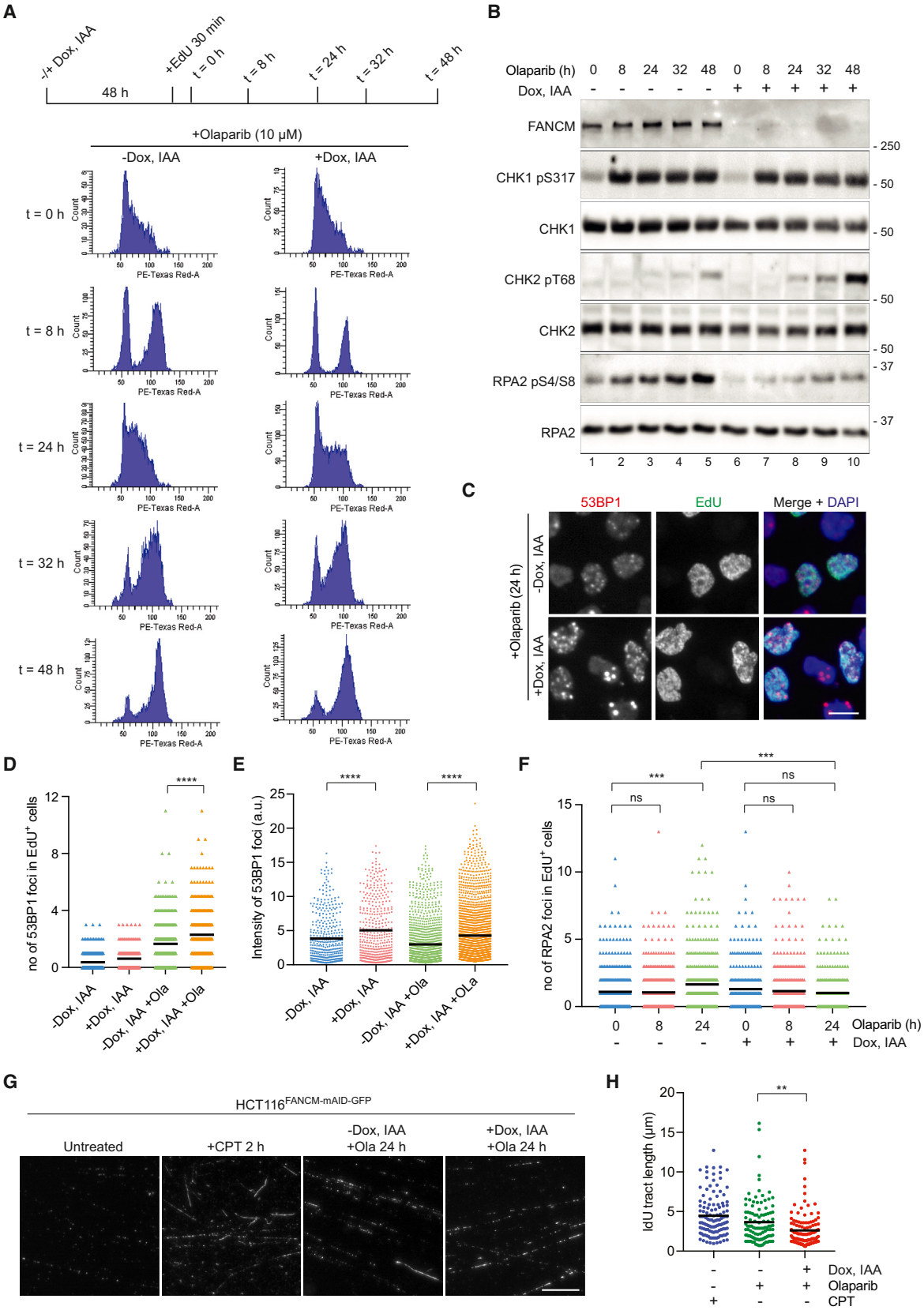

(legend on next page)

FANCM prevents the formation of 53BP1 foci and promotes resection

To verify the increased DDR and DNA damage in the second S phase, we quantified the number of phosphorylated ATM (ATM-pS1981) and 53BP1 foci. HCT116$^{FANCM\text{-}mAID\text{-}GFP}$ cells (±Dox, IAA) were treated with olaparib for 24 h, and S phase cells were EdU labeled (30 min). We observed a significant increase in the numbers of both ATM-pS1981 and 53BP1 foci in EdU$^+$-FANCM-depleted cells compared to EdU$^+$-mock-depleted cells (Figures 3C, 3D, S3A, and S3B). These results indicate that when FANCM-depleted cells initially in the S phase progress to the next S phase in the presence of olaparib, more DSBs are induced compared to mock-depleted cells. Importantly, the average fluorescence intensity of 53BP1 foci in FANCM-depleted cells was significantly higher than that of mock-depleted cells, with or without olaparib treatment (Figure 3E). These results suggest that FANCM may counteract 53BP1 recruitment to the DNA damage sites.

The decrease in RPA2-pS4/S8 observed in FANCM-depleted cells (Figure 3B) implies that upon PARPi treatment, FANCM is involved in promoting the resection of DSBs resulting from fork collapse in the second S phase. To further investigate this, we quantified the number of RPA2 foci in cells treated with olaparib (for 8 and 24 h) and labeled with EdU (30 min). In EdU$^+$-mock-depleted cells, the level of RPA2 foci significantly increased after 24 h of olaparib treatment, suggesting an increase in DNA end resection, leading to ssDNA formation (Figure 3F). Although olaparib treatment has been shown to induce an increased formation of ssDNA gaps in the first S phase,[21,22,29] we did not observe a significant increase in RPA2 foci after 8 h of olaparib treatment in EdU$^+$-mock-depleted cells (Figure 3F). This is likely due to our RPA2 staining not being sensitive enough to detect small ssDNA gaps. However, end resection of collapsed forks in the second S phase results in more extensive ssDNA formation, which can be detected as RPA2 foci. Notably, we did not observe an increase in RPA2 foci formation in EdU$^+$-FANCM-depleted cells after 24 h of olaparib treatment (Figure 3F).

To further support the notion that FANCM depletion impedes DNA resection following fork collapse, we employed the single-molecule analysis of resection tracks assay to visualize resection. DNA was labeled with IdU for 24 h before olaparib treatment. CPT treatment was included as a positive control. Both CPT and olaparib treatments generated distinct native IdU tracts (Figure 3G). FANCM depletion led to a significant reduction in the length of native IdU tracts upon olaparib treatment (Figures 3G and 3H). We further validated these results by conducting native BrdU immunofluorescence to detect ssDNA. Olaparib treatment caused a substantial increase in nuclear BrdU intensity. Notably, FANCM-depleted cells exhibited a significant decrease in nuclear BrdU intensity compared to mock-depleted cells (Figures S3D and S3E). Collectively, these results suggest that FANCM depletion prevents DNA end resection of DNA breaks induced by olaparib treatment.

FANCM promotes the repair of PARPi-induced damage by counteracting 53BP1

To rule out the possibility that an increased DDR in the absence of FANCM is due to increased PARP1 trapping, we examined the level of chromatin-bound PARP1 and showed that FANCM depletion did not impact the level of PARP1 trapping (Figure S3C).

To explore the mechanism through which FANCM promotes PARPi resistance, we knocked out PARP1 or 53BP1 in HCT116$^{FANCM\text{-}mAID\text{-}GFP}$ cells (Figure S4A). Notably, the loss of PARP1 completely rescued the olaparib hypersensitivity observed in FANCM-depleted cells (Figure 4A). These findings suggest that FANCM plays a crucial role in repairing DNA lesions induced by PARP1 trapping. Intriguingly, hypersensitivity to PARPis (olaparib and veliparib) in FANCM-depleted cells could also be significantly mitigated by 53BP1 knockout (Figures 4B and S4B). We confirmed the rescue effect using another clone of HCT116$^{FANCM\text{-}mAID\text{-}GFP}$ *53BP1*$^{-/-}$ cells (Figures S4C and S4D). The loss of 53BP1 is known to promote DNA end resection and restore HR. Since FANCM-depleted cells are HR proficient (Figure 2C), the rescue effect of 53BP1 deletion cannot be solely attributed to HR restoration. We hypothesize that FANCM may inhibit other 53BP1 functions in response to PARP1 trapping. Another possibility is that FANCM counteracts 53BP1's role in resection inhibition specifically at collapsed forks in the S phase, meaning that HR-mediated repair of I-SceI-induced DSBs would not be affected by FANCM depletion.

Next, we investigated the DDR of FANCM-depleted cells with a knockout of PARP1 or 53BP1. Cells were treated with olaparib at various time points (0, 24, and 48 h). FANCM depletion increased the level of CHK2-pT68 while decreasing the level of RPA2-pS4/S8 (Figures 4C and 4D, lanes 2–3 vs. lanes 5–6). In FANCM-depleted cells, PARP1 knockout reduced olaparib-induced CHK2-pT68 (Figure 4C, lanes 5–6 vs. lanes 11–12), demonstrating that FANCM is necessary for repairing DNA lesions caused by PARP1 trapping. Since PARP1-trapping-induced

Figure 3. FANCM-depleted cells display a stronger DNA damage response but a lower level of ssDNA in the second S phase

(A) HCT116$^{FANCM\text{-}mAID\text{-}GFP}$ cells (±Dox, IAA) were pulse labeled with EdU and treated with olaparib (10 μM) for the indicated time points. The DNA content histograms of EdU-positive mock-depleted and FANCM-depleted cells at the indicated time points are shown.

(B) Cells (±Dox, IAA) were treated with olaparib for the indicated time points. Cell extracts were analyzed by western blotting for the indicated proteins.

(C) Cells (±Dox, IAA) were treated with olaparib for 24 h and then treated with EdU (10 μM) for 30 min. 53BP1 (red), EdU (green), and DNA (blue) are visualized.

(D) Quantification of the number of 53BP1 foci in EdU-positive cells (>180 cells per condition) as visualized in (C).

(E) Quantification of the fluorescence intensity of 53BP1 foci (>400 foci per condition) as visualized in (C).

(F) Quantification of the number of RPA2 foci in EdU-positive cells (>240 cells per condition) treated as in (C) except RPA2 was stained instead of 53BP1.

(G) Cells (±Dox, IAA) were treated with IdU. Cells were then treated with CPT or olaparib. DNA fibers were stained with IdU under native conditions. Scale bars, 10 μm.

(H) Quantification of IdU tract length (>100 fibers per condition) from cells treated as in (G). The black lines represent the mean. *p* values were determined using an unpaired two-tailed t test.

See also Figure S3.

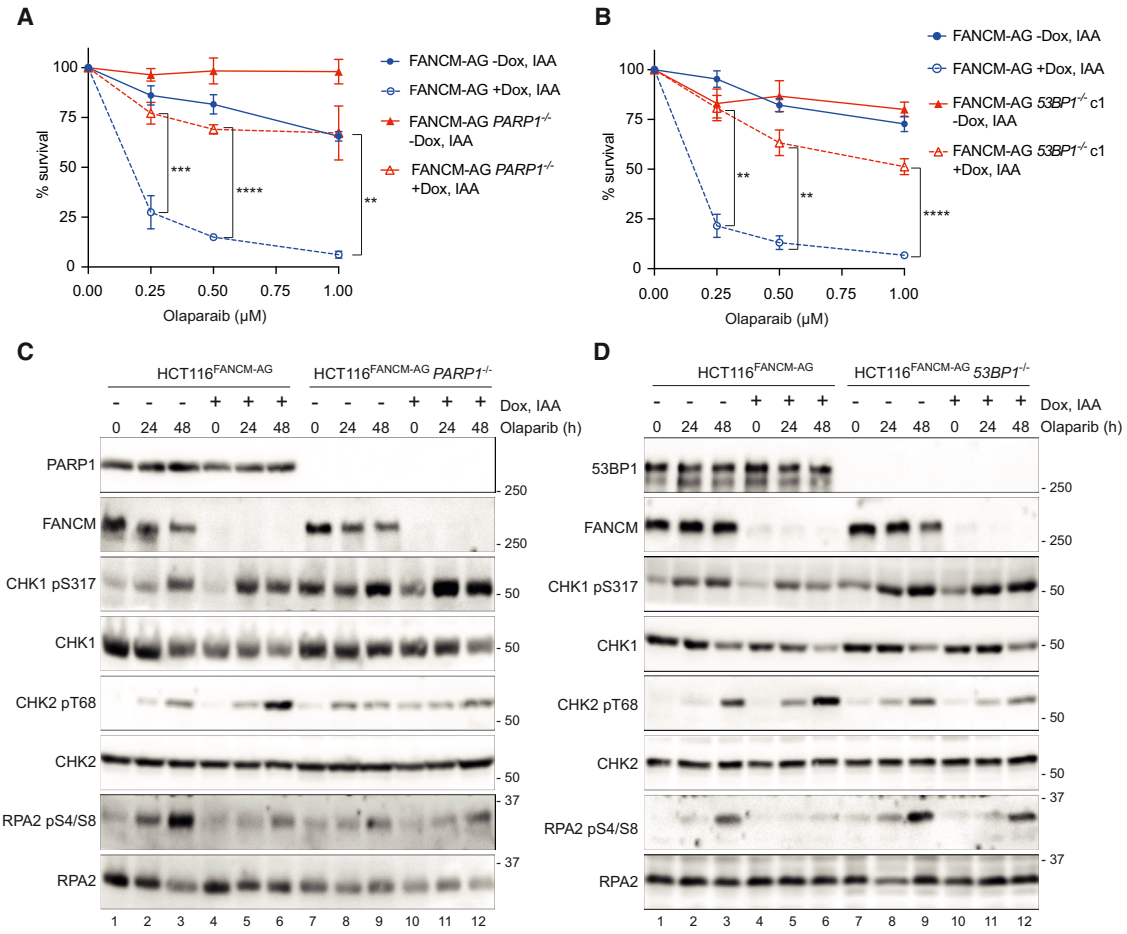

Figure 4. Knockout PARP1 or 53BP1 rescues PARPi sensitivity in FANCM-depleted cells

(A) Clonogenic cell survival assays were carried out on HCT116$^{FANCM\text{-}mAID\text{-}GFP}$ cells (FANCM-AG ± Dox, IAA) and HCT116$^{FANCM\text{-}mAID\text{-}GFP}$ *PARP1*$^{-/-}$ cells (FANCM-AG *PARP1*$^{-/-}$ ± Dox, IAA) treated with indicated concentrations of olaparib.

(B) Clonogenic cell survival assays were carried out on FANCM-AG cells (±Dox, IAA) and HCT116$^{FANCM\text{-}mAID\text{-}GFP}$ *53BP1*$^{-/-}$ cells (FANCM-AG *53BP1*$^{-/-}$ ± Dox, IAA) treated with indicated concentrations of olaparib.

(C) HCT116$^{FANCM\text{-}AG}$ cells and HCT116$^{FANCM\text{-}AG}$ *PARP1*$^{-/-}$ cells (±Dox, IAA) were treated with olaparib (10 μM) for the indicated time points. Cell extracts were analyzed by western blotting for the indicated proteins.

(D) HCT116$^{FANCM\text{-}AG}$ cells and HCT116$^{FANCM\text{-}AG}$ *53BP1*$^{-/-}$ cells (±Dox, IAA) were treated with olaparib for the indicated time points. Cell extracts were analyzed by western blotting for the indicated proteins.

Data in (A) and (B) are represented as mean ± SD, $n = 3$ independent experiments. p values were determined using an unpaired two-tailed t test.

See also Figure S4.

DNA damage would not occur in the absence of PARP1, there was no increase in resection-induced RPA2-pS4/S8 in *PARP1*$^{-/-}$ cells (Figure 4C, lanes 2–3 vs. lanes 8–9). Similarly, there was no difference in olaparib-induced CHK2-pT68 and RPA2-pS4/S8 between mock-depleted and FANCM-depleted cells upon olaparib treatment when PARP1 was knocked out (Figure 4C, lanes 8–9 vs. lanes 11–12).

53BP1$^{-/-}$/FANCM-depleted cells exhibited a reduced level of olaparib-induced CHK2-pT68 compared to *53BP1*$^{+/+}$/FANCM-depleted cells (Figure 4D, lanes 5–6 vs. lanes 11–12), indicating that the increased DNA damage in FANCM-depleted cells upon olaparib treatment is dependent on 53BP1. Knockout of 53BP1 elevated olaparib-induced RPA2-pS4/S8, while the CHK2-pT68 level remained similar (Figure 4D, lanes 2–3 vs. lanes 8–9), consistent with 53BP1's role in inhibiting resection. Importantly, knocking out 53BP1 in FANCM-depleted cells fully rescued the reduced level of olaparib-induced RPA2-pS4/S8 in *53BP1*$^{+/+}$/FANCM-depleted cells (Figure 4D, lanes 5–6 vs. lanes 11–12), suggesting that DNA end resection in FANCM-depleted cells is restored in the absence of 53BP1.

FANCM depletion induces ssDNA gaps behind the replication forks

It has been shown that upon PARPi treatment, ssDNA gaps are generated behind replication forks. These ssDNA gaps persist into the second S phase, leading to fork collapse and DSBs.[21,22,29] The increased DNA damage observed in olaparib-treated FANCM-depleted cells suggests that FANCM prevents

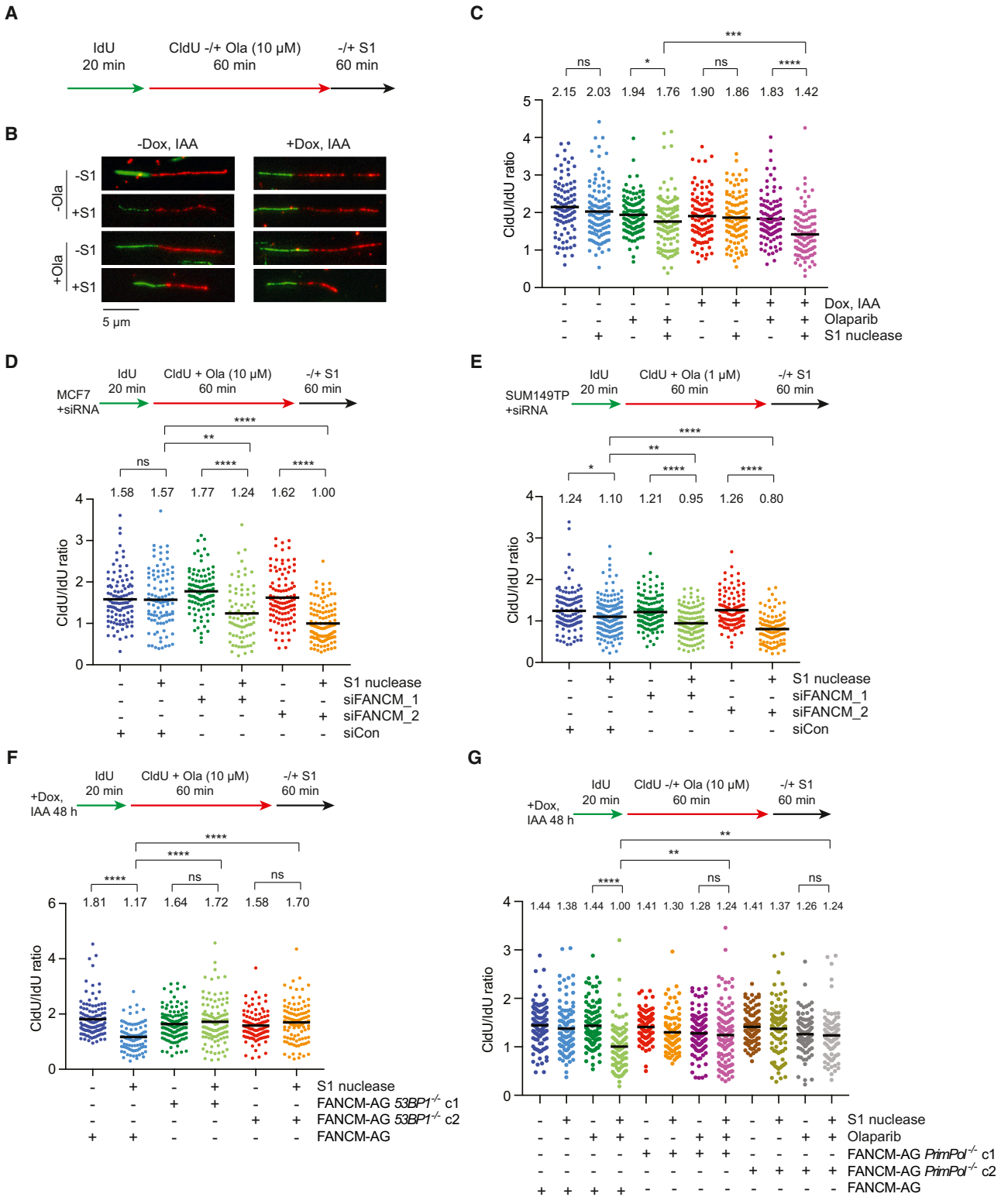

Figure 5. Depletion of FANCM induces increased formation of ssDNA gaps

(A) The experimental design for DNA fiber assay.

(B) Representative DNA fibers treated with or without S1 nuclease. Scale bar, 5 μm.

(legend continued on next page)

the formation of such ssDNA gaps. To test this possibility, we performed DNA fiber assays for HCT116$^{FANCM\text{-}mAID\text{-}GFP}$ cells with or without S1 nuclease, which specifically cleaves ssDNA (Figure 5A). When S1 nuclease cuts the ssDNA gaps behind the forks induced by olaparib, the CldU tracts shorten, resulting in a decreased CldU/IdU ratio of tract length. As anticipated, without olaparib, there was no significant difference in the CldU/IdU ratio between S1-untreated and S1-treated DNA fibers in either mock-depleted or FANCM-depleted cells (Figures 5B and 5C). The CldU/IdU ratio was significantly reduced by S1 treatment when cells were treated with olaparib, consistent with the notion that PARPis induce ssDNA gaps behind the replication forks. Notably, the CldU/IdU ratio in olaparib-treated FANCM-depleted cells with S1 treatment was further reduced when compared with olaparib-treated mocked-depleted cells with S1 treatment (Figure 5C, compare condition 4 with condition 8). These results indicate that more ssDNA gaps behind replication forks are present in FANCM-depleted cells upon PARPi treatment. We also confirmed this result by utilizing MCF-7 and SUM149PT cells, where FANCM was depleted by two independent siRNAs (Figures 5D and 5E). Consistent with the results obtained from HCT116$^{FANCM\text{-}mAID\text{-}GFP}$ cells, the CldU/IdU ratio in FANCM-depleted MCF-7 and SUM149PT cells treated with olaparib and S1 nuclease exhibited a significant reduction when compared to olaparib-treated mocked-depleted cells with S1 treatment (Figures 5D and 5E).

To investigate whether FANCM prevents ssDNA gap formation by counteracting 53BP1, we performed DNA fiber assays on HCT116$^{FANCM\text{-}mAID\text{-}GFP}$ and HCT116$^{FANCM\text{-}mAID\text{-}GFP}$ *53BP1*$^{-/-}$ cells treated with olaparib (Figure 5F). We observed that the reduction in the CldU/IdU ratio induced by FANCM depletion upon S1 treatment could be fully rescued by 53BP1 knockout (Figure 5F). Therefore, we conclude that FANCM is involved in limiting ssDNA gap accumulation in the first S phase after PARPi exposure by counteracting 53BP1 (Figure S5A).

A recent report demonstrated that detectable ssDNA gaps using the DNA fiber spreading assay indicate their formation on both leading and lagging strands.[83] Therefore, our DNA fiber assay results should imply the presence of ssDNA gaps on both strands in olaparib-treated FANCM-depleted cells. Considering PRIMPOL repriming generates ssDNA gaps in leading strands,[26,27,84–86] we generated the HCT116$^{FANCM\text{-}mAID\text{-}GFP}$ *PrimPol*$^{-/-}$ cell lines to investigate whether gaps on leading strands in olaparib-treated FANCM-depleted cells are PRIMPOL dependent. Two *PrimPol*$^{-/-}$ clones were confirmed by western blotting (Figure S5B). In the DNA fiber assay, we found that PRIMPOL knockout prevented ssDNA gap formation in FANCM-depleted cells treated with olaparib (Figure 5G, compare condition 4 with conditions 8 and 12).

Based on our model, we predict that enhancing DNA replication in the second S phase would induce more DNA damage and therefore further increase the PARPi sensitivity in FANCM-depleted cells. The ATR-CHK1 checkpoint pathway is well known for suppressing DNA synthesis in the presence of DNA damage.[87] To enhance origin firing in olaparib-treated cells, we treated cells with the ATR inhibitor VE-821. We treated HCT116$^{FANCM\text{-}mAID\text{-}GFP}$ cells (+Dox, IAA) for 4 or 28 h and exposed cells to VE-821 in the last 4 h (Figure S5C). VE-821 almost completely abolished CHK1 activation (Figure S5C). Importantly, inhibition of ATR by VE-821 induced an increase in CHK2 pT68 after 28 h of olaparib treatment, suggesting that unrestricted origin firing induces more DNA damage upon olaparib treatment. Furthermore, we treated HCT116$^{FANCM\text{-}mAID\text{-}GFP}$ cells (+Dox, IAA) with a dose of VE-821, which has a minor effect on cell survival, and a dose of olaparib that induced ~50% reduction of survival. Combined treatment of VE-821 and olaparib displayed a synergistic effect with ~95% loss of cell survival (Figure S5D). These results suggest that unrestricted DNA synthesis leads to higher PARPi sensitivity in FANCM-depleted cells.

FANCM has distinct roles in the first and second S phases upon PARPi treatment

Since deletion of 53BP1 rescues both the increase in DNA damage induction and the reduced level of resection, we speculate that FANCM counteracts the actions of 53BP1 in both the first and second S phases upon PARPi exposure (Figure S5A). To test this, we specifically depleted FANCM in the first and second cell cycles using our auxin-inducible degron cells. The depletion of FANCM-mAID-GFP was reversible, as removing Dox and IAA for 16–24 h fully restored the protein expression (Figure 6A). We synchronized HCT116$^{FANCM\text{-}mAID\text{-}GFP}$ cells with four different schemes (Figure 6B): (1) cells (−Dox and IAA) were treated with a CDK1 inhibitor RO-3306 (to arrest cells in the G2 phase) and olaparib for 20 h. They were then released into fresh media for 16 h so that some cells entered the next S phase. In this scheme, cells expressed FANCM continuously. (2) Cells were treated with Dox and IAA for 24 h followed by RO-3306 and olaparib for 20 h. They were then released into media containing Dox and IAA for 16 h. In this scheme, cells were depleted with FANCM in both cell cycles. (3) Cells were treated with Dox and IAA for 24 h followed by RO-3306 and olaparib for 20 h. They were then released into media (−Dox, IAA) for 16 h. In this scheme, cells were depleted with FANCM in the first cell cycle,

(C) Quantification of the CldU/IdU double-labeled DNA tracts from HCT116$^{FANCM\text{-}mAID\text{-}GFP}$ cells treated as in (A). More than 100 DNA fibers were analyzed in each condition.
(D) Quantification of the CldU/IdU double-labeled DNA tracts from MCF-7 cells treated as indicated. More than 100 DNA fibers were analyzed in each condition.
(E) Quantification of the CldU/IdU double-labeled DNA tracts from SUM149PT cells treated as indicated. More than 100 DNA fibers were analyzed in each condition.
(F) Quantification of the CldU/IdU double-labeled DNA tracts from HCT116$^{FANCM\text{-}mAID\text{-}GFP}$ cells (FANCM-AG) and FANCM-AG *53BP1*$^{-/-}$ cells treated as indicated. More than 100 DNA fibers were analyzed in each condition.
(G) Quantification of the CldU/IdU double-labeled DNA tracts from FANCM-AG cells and FANCM-AG *PrimPol*$^{-/-}$ cells treated as indicated. More than 100 DNA fibers were analyzed in each condition. The black lines represent the mean. The mean values of the CldU/IdU ratio are displayed at the top of the graphs. *p* values were determined using an unpaired two-tailed t test.
See also Figure S5.

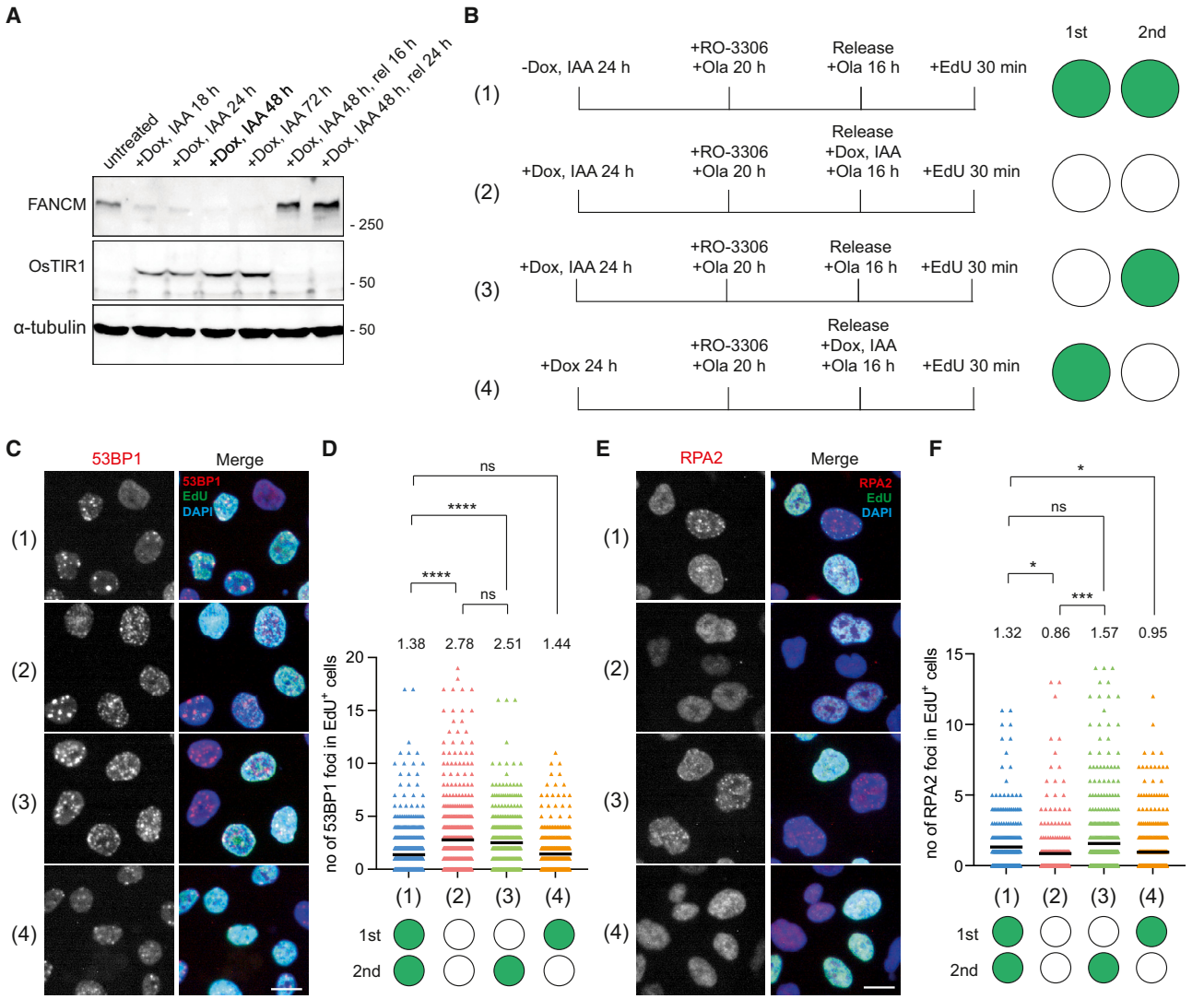

Figure 6. FANCM plays distinct roles in the first and second S phases

(A) HCT116$^{FANCM\text{-}mAID\text{-}GFP}$ cells were treated with Dox and IAA at the indicated time points. Cells were washed and released to fresh media for 16 or 20 h. Cell extracts were analyzed by western blotting.

(B) Schematic workflows for (1) not depleting FANCM and depleting FANCM (2) in both cell cycles, (3) only in the first cell cycle, and (4) only in the second cell cycle. The green circles represent cells expressing FANCM. The white circles represent cells depleted of FANCM.

(C) Cells were treated as in (B). 53BP1 (red), EdU (green), and DNA (blue) are visualized.

(D) Quantification of the number of 53BP1 foci in EdU-positive cells (>420 cells per condition) as visualized in (C).

(E) Cells were treated as in (B). RPA2 (red), EdU (green), and DNA (blue) are visualized. Scale bars, 10 μm.

(F) Quantification of the number of RPA2 foci in EdU-positive cells (>330 cells per condition) as visualized in (E). The black lines represent the mean. The mean values of the foci number are displayed at the top of the graphs. *p* values were determined using an unpaired two-tailed t test.

See also Figure S6.

but FANCM was re-expressed when entering the second S phase. (4) Cells were treated only with Dox for 24 h followed by RO-3306 and olaparib for 20 h. They were then released into media containing Dox and IAA for 16 h. In this scheme, cells expressed FANCM in the first cell cycle, but FANCM was induced to be degraded when entering the second S phase. We confirmed the depletion and expression of FANCM in the first and second cell cycles by western blotting (Figure S6A). Fluorescence-activated cell sorting analyses confirmed that most cells were arrested in the G2 phase upon RO-3306 treatment and released into the next cell cycle (Figure S6B). However, a small proportion of cells were either unable to be arrested in G2 upon RO-3306 treatment or unable to be released from G2. Therefore, to make sure only S-phase cells were examined, we labeled them with EdU before staining. We examined the number of 53BP1 and RPA2 foci, which indicate DNA damage and resection-generated ssDNA, respectively. EdU$^+$ cells in schemes 2 and 3 exhibited significantly higher levels of 53BP1 foci

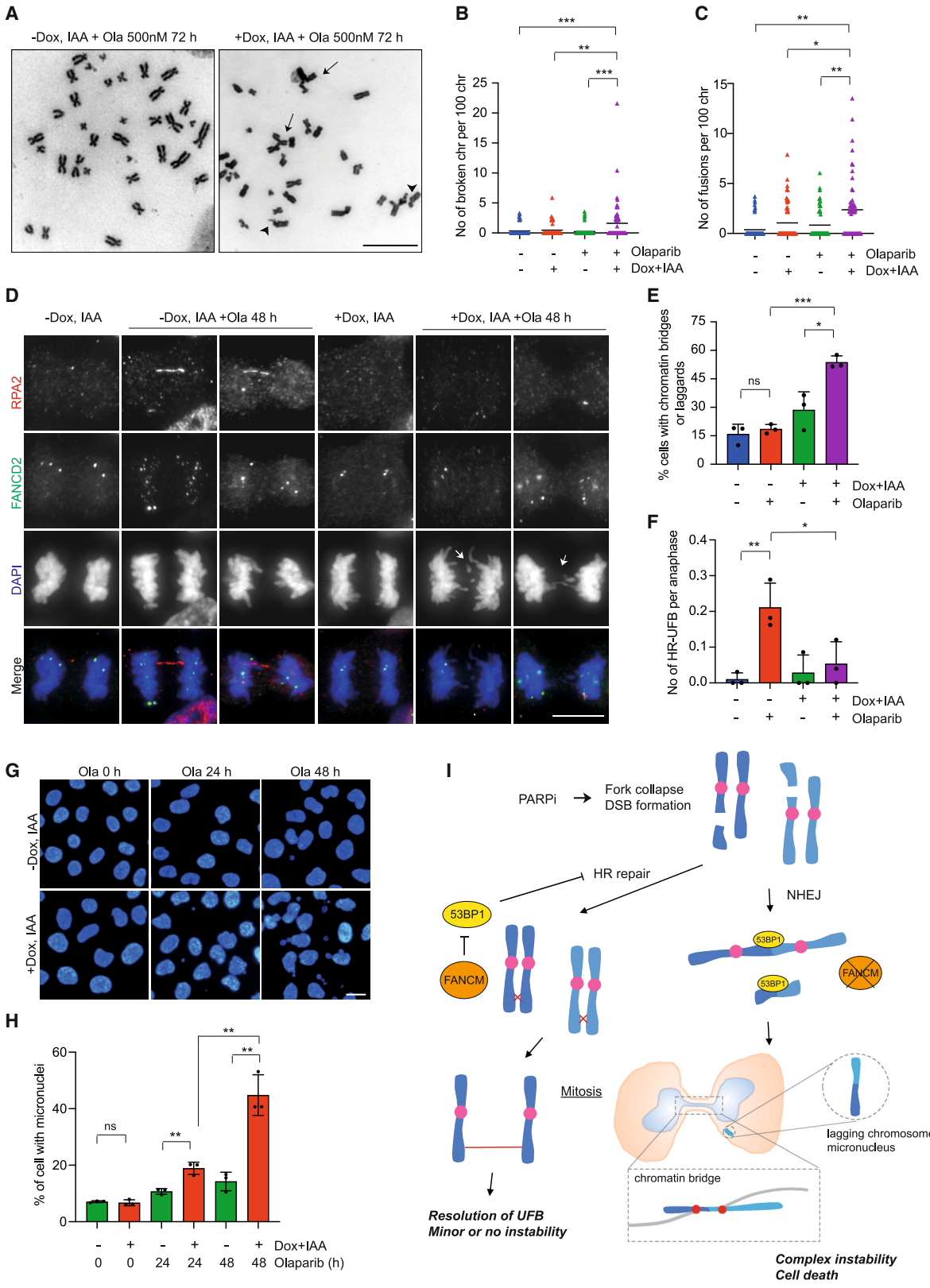

(legend on next page)

compared with those of schemes 1 and 4. There was no significant difference in the number of 53BP1 foci between schemes 2 and 3 (Figures 6C and 6D). These results indicate that FANCM is required in the first S phase to prevent the formation of excessive DSBs in the second S phase. Similarly, EdU^+ cells in schemes 2 and 4 exhibited significantly reduced levels of RPA2 foci when compared with those of schemes 1 and 3 (Figures 6E and 6F), indicating that re-expression of FANCM in the second S phase is sufficient to promote resection of collapsed forks.

PARPi induces chromosomal instability in FANCM-depleted cells

Our results suggested that in the absence of FANCM, 53BP1 inhibits DNA end resection at the collapsed forks. Therefore, PARPi-induced DSBs would likely be repaired through the non-homologous end joining (NHEJ) pathway, which may result in broken chromosomes and chromosome fusions (both end-to-end and radial chromosomes). To measure chromosomal aberrations induced by olaparib in FANCM-depleted cells, we performed chromosome spread analyses to quantify broken chromosomes and fusions. Upon olaparib treatment, FANCM-depleted cells displayed a significant increase in the formation of aberrant chromosomes compared with untreated or mock-depleted cells (Figures 7A–7C). We hypothesize that NHEJ-mediated repair produces dicentric and acentric chromosomes, which induce chromosome segregation defects in olaparib-treated FANCM-depleted cells. Therefore, we quantified the formation of chromatin bridges (arising from dicentrics) and lagging chromosomes (arising from acentrics). As expected, after 48 h of olaparib treatment, a higher frequency of chromosome segregation defects in FANCM-depleted cells was observed compared with mock-depleted cells (Figures 7D and 7E). Moreover, we expect that resection of olaparib-induced collapsed forks followed by HR-mediated repair occurs in the presence of FANCM. HR repair could generate recombination intermediates that lead to HR-ultrafine anaphase bridges (HR-UFBs) in the subsequent mitosis.[88,89] Therefore, we measured the frequency of HR-UFBs as a marker of HR repair. HR-UFBs are characterized by their frequent conversion to ssDNA bridges (i.e., RPA coated) and the absence of FANCD2 foci at their termini.[88,89] We co-stained RPA2 and FANCD2 and indeed found that mock-depleted cells treated with olaparib (48 h) displayed a significantly higher frequency of HR-UFBs compared with untreated cells (Figures 7D and 7F). Importantly, FANCM depletion led to a significantly reduced level of olaparib-induced HR-UFBs. These results support our model that FANCM plays a crucial role in promoting the repair of collapsed forks induced by PARPis through HR rather than NHEJ (Figure 7I).

Next, we measured the frequency of micronuclei formation. Upon olaparib treatment, FANCM-depleted cells exhibited a significant increase in micronuclei formation compared with mock-depleted cells (Figures 7G and 7H). A much larger increase was observed after 48 h olaparib treatment than after 24 h, suggesting that the chromosome segregation defects primarily occur in the second mitosis. Micronuclei can be formed due to the breakage of dicentric chromatin bridges, acentric fragments, or unattached kinetochores. To determine the origin of the observed micronuclei, we quantified the percentage of micronuclei with or without centromeres. The percentage of micronuclei containing acentric chromosome fragments was significantly increased in FANCM-depleted cells treated with olaparib compared with mock-depleted cells (Figures S7A and S7B). This indicates that the increase in micronuclei was due to either the breakage of chromatin bridges or the missegregation of acentric chromosomes (Figure 7I). Importantly, we showed that olaparib-induced micronuclei in FANCM-depleted cells could be rescued by 53BP1 knockout (Figure S7C), confirming the notion that the key function of FANCM is to counteract 53BP1.

FANCM is known to interact with MHF1 and MHF2, which are constitutive centromere proteins (also referred to as CENP-S and CENP-X).[81,90,91] To test whether FANCM plays a direct role regulating chromosome segregation, we first examined the sensitivity of FANCM-depleted cells to low doses of nocodazole, a drug known to cause chromosome segregation defects. The results showed no increased sensitivity to nocodazole in FANCM-depleted cells (Figure S7D). Next, we treated both mock-depleted and FANCM-depleted cells with nocodazole, followed by a 6 h release period, and then quantified the number of micronuclei containing centromere signals (an indicator of chromosome missegregation). FANCM depletion did not lead to an increase in the formation of micronuclei exhibiting centromere signals (Figure S7E). Collectively, these results suggest that FANCM does not directly regulate chromosome segregation.

DISCUSSION

Enhancing the effectiveness of PARPis in patients and expanding their applications beyond *BRCA*-mutated cancers requires a thorough understanding of how other DNA repair proteins influence PARPi resistance or sensitivity. Our results prompt us to

Figure 7. FANCM depletion induces chromosomal instability upon olaparib treatment

(A) Representative images of chromosome spreads of $HCT116^{FANCM\text{-}mAID\text{-}GFP}$ cells (±Dox, IAA) treated with olaparib. Arrowheads are pointing to broken chromosomes. Arrows are pointing to radial chromosomes.

(B and C) Quantification of broken chromosomes (B) and radial/fusion chromosomes (C) in chromosome spreads (60 spreads per condition, the black lines represent the mean) as visualized in (A).

(D) Cells (±Dox, IAA) were treated with or without olaparib (10 μM) for 48 h. RPA2 (red), FANCD2 (green), and DNA (blue) are visualized.

(E and F) Quantification of anaphase cells (>80 cells per condition) with chromatin bridges/lagging chromosomes (E) and RPA2-coated UFBs that are not associated with FANCD2 foci (F), as visualized in (D).

(G) Cells (±Dox, IAA) were treated with olaparib (10 μM) for the indicated time points. Scale bars, 10 μm.

(H) Quantification of cells with micronuclei (>2,300 cells per condition) as visualized in (G).

(I) A schematic showing how PARPis induce chromosomal instability in FANCM-depleted cells. See the main text for details.

Data in (E), (F), and (H) are represented as mean ± SD, $n = 3$ independent experiments. p values were determined using an unpaired two-tailed t test.

See also Figure S7.

propose a model wherein FANCM performs a dual function in repairing PARPi-induced lesions (Figure S5A). PARP1 trapping, induced by PARPis, hinders the processing of unligated Okazaki fragments. FANCM acts to prevent the formation of ssDNA gaps on lagging strands by counteracting 53BP1, which is known to inhibit Okazaki fragment processing.[22] PARPis also induce gap formation on the leading strands in FANCM-depleted cells via a PRIMPOL-dependent mechanism. In the second S phase, replication fork collisions with ssDNA gaps result in fork collapse and one-ended DSBs. Another role of FANCM involves facilitating the repair of collapsed forks through HR, as it promotes resection at collapsed forks by counteracting 53BP1, a known resection inhibitor.[49,50] In the absence of FANCM, 53BP1 inhibits resection, prompting error-prone repair via NHEJ to repair the collapsed forks. This leads to structural chromosomal instability, manifesting as radial chromosomes and chromatin bridges (Figure 7I).

Our model aligns with previous studies demonstrating that FANCM restricts ssDNA formation under replication stress independently of the core FA pathway. Several potential mechanisms could explain this function of FANCM. One possibility is that FANCM promotes the recovery of stalled replication forks through fork remodeling into reversed forks, preventing persistent fork stalling or collapse that would generate ssDNA. Stalled forks can also be restarted by repriming and reinitiating leading strand replication through PRIMPOL-generated ssDNAs.[26,27] Additionally, FANCM promotes ATR/CHK1 activation to facilitate fork recovery.[66,67,92] However, in FANCM-depleted cells treated with olaparib, we observed no difference in CHK1 phosphorylation, suggesting that FANCM does not impact ATR/CHK1 activation during PARPi treatment. Although FANCM depletion has been shown to induce increased DSB and ssDNA formation upon HU treatment,[65,66,93,94] FANCM-depleted cells do not exhibit an increased sensitivity to HU (Figure S1C). Moreover, HU caused a rapid increase in γH2AX/pCHK2 in FANCM-depleted cells within 1–6 h,[65,93] while olaparib treatment required 24 h to induce clear CHK2 phosphorylation. Therefore, the mechanisms of how FANCM-depleted cells respond to HU and PARPi are different. Importantly, the increased DNA damage and ssDNA gaps observed in FANCM-depleted cells can be rescued by knocking out 53BP1. Recent studies propose that 53BP1 interferes with XRCC1-dependent Okazaki fragment ligation, while BRCA1 inhibits gap accumulation by impeding 53BP1.[22] Similar to BRCA1, our results support the idea that FANCM restrains 53BP1 to limit ssDNA gap accumulation upon PARP inhibition. FANCM and BRCA1 may independently inhibit 53BP1, as their co-depletion results in a synergistic effect on PARPi-induced cell death. FANCM also counteracts 53BP1 to promote resection of the DSB ends generated from fork collapse in the second S phase. Previous research has shown that FANCM interacts with "stressed" replisomes,[72,95] which could explain its specific inhibition of resection at collapsed forks. The exact mechanism by which FANCM inhibits 53BP1 remains unclear. One simple explanation is that FANCM interferes with 53BP1 recruitment to stalled or collapsed forks. This hypothesis is supported by our observation that FANCM depletion increases 53BP1 foci intensity. The translocase activity of FANCM may remodel replication forks upon encountering ssDNA gaps, thereby interfering with 53BP1 recruitment.

RPA exhaustion and under-replicated DNA induced by PARPis may induce replication stress, leading to mitotic defects and cell death.[21,22,30–32,96] In FANCM-depleted cells, we also observed a significant increase in chromosomal abnormalities and segregation defects. However, these defects are not directly triggered by ssDNA-gap-induced replication stress. Instead, we propose that DSBs converted from ssDNA gaps are primarily repaired by NHEJ due to the lack of resection in the absence of FANCM. The chromosomal abnormalities induced by NHEJ account for the mitotic defects observed in PARPi-treated FANCM-depleted cells.

Although FANCM was identified as a core component of the FA pathway, individuals with biallelic FANCM mutations did not develop FA.[97,98] Instead, they experienced early-onset cancers, and cells derived from these patients exhibited a high degree of chromosomal instability. Furthermore, homozygous *FANCM* truncating variants have been linked to an increased risk of breast cancer.[77] Our study sheds light on how FANCM contributes to PARPi resistance and has several important implications. Firstly, FANCM-deficient cells, despite being HR proficient, display hypersensitivity to PARPis. This suggests that PARPis could be applied to HR-proficient tumors. Secondly, FANCM merits further investigation by analyzing data from patients with cancer to determine if it can serve as a biomarker and molecular determinant for cancer treatment using PARPis. Lastly, our project indicates that FANCM inhibition could potentially be combined with PARPi therapy for both HR-proficient and HR-defective tumors.

Limitations of the study

We identified ssDNA gaps induced by FANCM depletion using a DNA fiber spreading assay. However, this technique has certain limitations, as it can only detect the shortening of DNA fibers when ssDNA gaps are present on both leading and lagging strands. Therefore, our understanding of the precise mechanism by which FANCM depletion promotes gap formation remains incomplete. Future studies should consider employing alternative methodologies, such as DNA combing, to complement the findings from our current investigation.

STAR★METHODS

Detailed methods are provided in the online version of this paper and include the following:

- KEY RESOURCES TABLE
- RESOURCE AVAILABILITY
  - Lead contact
  - Materials availability
  - Data and code availability
- EXPERIMENTAL MODEL AND STUDY PARTICIPANT DETAILS
- METHOD DETAILS
  - Plasmid construction
  - Transfection and cell line generation
  - RNA interference
  - Genomic PCR
  - Antibodies
  - Protein extraction and western blotting

- Flow cytometry
- Immunofluorescence and microscopy
- Clonogenic cell survival and cell variability assays
- Metaphase spread
- SMART assay
- Native BrdU staining
- DNA fiber analysis with S1 nuclease treatment

- QUANTIFICATION AND STATISTICAL ANALYSIS

SUPPLEMENTAL INFORMATION

Supplemental information can be found online at https://doi.org/10.1016/j.celrep.2024.114464.

ACKNOWLEDGMENTS

We thank Stephen West for the reagents. We thank Wai Hung Sit for technical assistance. The work is supported by the Guangdong Basic and Applied Basic Research Foundation from the Guangdong Provincial Department of Science and Technology (project no. 2021A1515010437), the Research Grant Council of Hong Kong (project no. ECS27110120), and the University of Hong Kong.

AUTHOR CONTRIBUTIONS

Y.W.C. conceived the study. Z.L., H.J., and S.Y.L. conducted the experiments. N.K. generated the FANCM auxin-degron cells. Y.W.C. and Z.L. wrote the manuscript.

DECLARATION OF INTERESTS

The authors declare no competing interests.

Received: December 19, 2023
Revised: May 22, 2024
Accepted: June 24, 2024
Published: July 8, 2024

REFERENCES

1. Farmer, H., McCabe, N., Lord, C.J., Tutt, A.N.J., Johnson, D.A., Richardson, T.B., Santarosa, M., Dillon, K.J., Hickson, I., Knights, C., et al. (2005). Targeting the DNA repair defect in BRCA mutant cells as a therapeutic strategy. Nature *434*, 917–921. https://doi.org/10.1038/nature03445.
2. Bryant, H.E., Schultz, N., Thomas, H.D., Parker, K.M., Flower, D., Lopez, E., Kyle, S., Meuth, M., Curtin, N.J., and Helleday, T. (2005). Specific killing of BRCA2-deficient tumours with inhibitors of poly(ADP-ribose) polymerase. Nature *434*, 913–917. https://doi.org/10.1038/nature03443.
3. Chen, C.C., Feng, W., Lim, P.X., Kass, E.M., and Jasin, M. (2018). Homology-Directed Repair and the Role of BRCA1, BRCA2, and Related Proteins in Genome Integrity and Cancer. Annu. Rev. Cancer Biol. *2*, 313–336. https://doi.org/10.1146/annurev-cancerbio-030617-050502.
4. Lord, C.J., and Ashworth, A. (2016). BRCAness revisited. Nat. Rev. Cancer *16*, 110–120. https://doi.org/10.1038/nrc.2015.21.
5. Min, A., Im, S.A., Yoon, Y.K., Song, S.H., Nam, H.J., Hur, H.S., Kim, H.P., Lee, K.H., Han, S.W., Oh, D.Y., et al. (2013). RAD51C-deficient cancer cells are highly sensitive to the PARP inhibitor olaparib. Mol. Cancer Ther. *12*, 865–877. https://doi.org/10.1158/1535-7163.MCT-12-0950.
6. Loveday, C., Turnbull, C., Ramsay, E., Hughes, D., Ruark, E., Frankum, J.R., Bowden, G., Kalmyrzaev, B., Warren-Perry, M., Snape, K., et al. (2011). Germline mutations in RAD51D confer susceptibility to ovarian cancer. Nat. Genet. *43*, 879–882. https://doi.org/10.1038/ng.893.
7. McCabe, N., Turner, N.C., Lord, C.J., Kluzek, K., Bialkowska, A., Swift, S., Giavara, S., O'Connor, M.J., Tutt, A.N., Zdzienicka, M.Z., et al. (2006). Deficiency in the repair of DNA damage by homologous recombination and sensitivity to poly(ADP-ribose) polymerase inhibition. Cancer Res. *66*, 8109–8115. https://doi.org/10.1158/0008-5472.CAN-06-0140.
8. Fugger, K., Bajrami, I., Silva Dos Santos, M., Young, S.J., Kunzelmann, S., Kelly, G., Hewitt, G., Patel, H., Goldstone, R., Carell, T., et al. (2021). Targeting the nucleotide salvage factor DNPH1 sensitizes BRCA-deficient cells to PARP inhibitors. Science *372*, 156–165. https://doi.org/10.1126/science.abb4542.
9. Menezes, M.C.S., Raheem, F., Mina, L., Ernst, B., and Batalini, F. (2022). PARP Inhibitors for Breast Cancer: Germline BRCA1/2 and Beyond. Cancers *14*, 4332. https://doi.org/10.3390/cancers14174332.
10. Serrano-Benitez, A., Wells, S.E., Drummond-Clarke, L., Russo, L.C., Thomas, J.C., Leal, G.A., Farrow, M., Edgerton, J.M., Balasubramanian, S., Yang, M., et al. (2023). Unrepaired base excision repair intermediates in template DNA strands trigger replication fork collapse and PARP inhibitor sensitivity. EMBO J. *42*, e113190. https://doi.org/10.15252/embj.2022113190.
11. Schlacher, K., Wu, H., and Jasin, M. (2012). A distinct replication fork protection pathway connects Fanconi anemia tumor suppressors to RAD51-BRCA1/2. Cancer Cell *22*, 106–116. https://doi.org/10.1016/j.ccr.2012.05.015.
12. Schlacher, K., Christ, N., Siaud, N., Egashira, A., Wu, H., and Jasin, M. (2011). Double-strand break repair-independent role for BRCA2 in blocking stalled replication fork degradation by MRE11. Cell *145*, 529–542. https://doi.org/10.1016/j.cell.2011.03.041.
13. Hashimoto, Y., Ray Chaudhuri, A., Lopes, M., and Costanzo, V. (2010). Rad51 protects nascent DNA from Mre11-dependent degradation and promotes continuous DNA synthesis. Nat. Struct. Mol. Biol. *17*, 1305–1311. https://doi.org/10.1038/nsmb.1927.
14. Michelena, J., Lezaja, A., Teloni, F., Schmid, T., Imhof, R., and Altmeyer, M. (2018). Analysis of PARP inhibitor toxicity by multidimensional fluorescence microscopy reveals mechanisms of sensitivity and resistance. Nat. Commun. *9*, 2678. https://doi.org/10.1038/s41467-018-05031-9.
15. Murai, J., Huang, S.y.N., Das, B.B., Renaud, A., Zhang, Y., Doroshow, J.H., Ji, J., Takeda, S., and Pommier, Y. (2012). Trapping of PARP1 and PARP2 by Clinical PARP Inhibitors. Cancer Res. *72*, 5588–5599. https://doi.org/10.1158/0008-5472.CAN-12-2753.
16. Maya-Mendoza, A., Moudry, P., Merchut-Maya, J.M., Lee, M., Strauss, R., and Bartek, J. (2018). High speed of fork progression induces DNA replication stress and genomic instability. Nature *559*, 279–284. https://doi.org/10.1038/s41586-018-0261-5.
17. Ho, Y.C., Ku, C.S., Tsai, S.S., Shiu, J.L., Jiang, Y.Z., Miriam, H.E., Zhang, H.W., Chen, Y.T., Chiu, W.T., Chang, S.B., et al. (2022). PARP1 recruits DNA translocases to restrain DNA replication and facilitate DNA repair. PLoS Genet. *18*, e1010545. https://doi.org/10.1371/journal.pgen.1010545.
18. Ray Chaudhuri, A., and Nussenzweig, A. (2017). The multifaceted roles of PARP1 in DNA repair and chromatin remodelling. Nat. Rev. Mol. Cell Biol. *18*, 610–621. https://doi.org/10.1038/nrm.2017.53.
19. Berti, M., Ray Chaudhuri, A., Thangavel, S., Gomathinayagam, S., Kenig, S., Vujanovic, M., Odreman, F., Glatter, T., Graziano, S., Mendoza-Maldonado, R., et al. (2013). Human RECQ1 promotes restart of replication forks reversed by DNA topoisomerase I inhibition. Nat. Struct. Mol. Biol. *20*, 347–354. https://doi.org/10.1038/nsmb.2501.
20. Ray Chaudhuri, A., Hashimoto, Y., Herrador, R., Neelsen, K.J., Fachinetti, D., Bermejo, R., Cocito, A., Costanzo, V., and Lopes, M. (2012). Topoisomerase I poisoning results in PARP-mediated replication fork reversal. Nat. Struct. Mol. Biol. *19*, 417–423. https://doi.org/10.1038/nsmb.2258.
21. Panzarino, N.J., Krais, J.J., Cong, K., Peng, M., Mosqueda, M., Nayak, S.U., Bond, S.M., Calvo, J.A., Doshi, M.B., Bere, M., et al. (2021). Replication Gaps Underlie BRCA Deficiency and Therapy Response. Cancer Res. *81*, 1388–1397. https://doi.org/10.1158/0008-5472.CAN-20-1602.

22. Cong, K., Peng, M., Kousholt, A.N., Lee, W.T.C., Lee, S., Nayak, S., Krais, J., VanderVere-Carozza, P.S., Pawelczak, K.S., Calvo, J., et al. (2021). Replication gaps are a key determinant of PARP inhibitor synthetic lethality with BRCA deficiency. Mol. Cell *81*, 3128–3144.e7. https://doi.org/10.1016/j.molcel.2021.06.011.

23. Belan, O., Sebald, M., Adamowicz, M., Anand, R., Vancevska, A., Neves, J., Grinkevich, V., Hewitt, G., Segura-Bayona, S., Bellelli, R., et al. (2022). POLQ seals post-replicative ssDNA gaps to maintain genome stability in BRCA-deficient cancer cells. Mol. Cell *82*, 4664–4680.e9. https://doi.org/10.1016/j.molcel.2022.11.008.

24. Vaitsiankova, A., Burdova, K., Sobol, M., Gautam, A., Benada, O., Hanzlikova, H., and Caldecott, K.W. (2022). PARP inhibition impedes the maturation of nascent DNA strands during DNA replication. Nat. Struct. Mol. Biol. *29*, 329–338. https://doi.org/10.1038/s41594-022-00747-1.

25. Hanzlikova, H., Kalasova, I., Demin, A.A., Pennicott, L.E., Cihlarova, Z., and Caldecott, K.W. (2018). The Importance of Poly(ADP-Ribose) Polymerase as a Sensor of Unligated Okazaki Fragments during DNA Replication. Mol. Cell *71*, 319–331.e3. https://doi.org/10.1016/j.molcel.2018.06.004.

26. Tirman, S., Quinet, A., Wood, M., Meroni, A., Cybulla, E., Jackson, J., Pegoraro, S., Simoneau, A., Zou, L., and Vindigni, A. (2021). Temporally distinct post-replicative repair mechanisms fill PRIMPOL-dependent ssDNA gaps in human cells. Mol. Cell *81*, 4026–4040.e8. https://doi.org/10.1016/j.molcel.2021.09.013.

27. Quinet, A., Tirman, S., Jackson, J., Šviković, S., Lemaçon, D., Carvajal-Maldonado, D., González-Acosta, D., Vessoni, A.T., Cybulla, E., Wood, M., et al. (2020). PRIMPOL-Mediated Adaptive Response Suppresses Replication Fork Reversal in BRCA-Deficient Cells. Mol. Cell *77*, 461–474.e9. https://doi.org/10.1016/j.molcel.2019.10.008.

28. Genois, M.M., Gagne, J.P., Yasuhara, T., Jackson, J., Saxena, S., Langelier, M.F., Ahel, I., Bedford, M.T., Pascal, J.M., Vindigni, A., et al. (2021). CARM1 regulates replication fork speed and stress response by stimulating PARP1. Mol Cell *81*, 784–800 e788. https://doi.org/10.1016/j.molcel.2020.12.010.

29. Simoneau, A., Xiong, R., and Zou, L. (2021). The trans cell cycle effects of PARP inhibitors underlie their selectivity toward BRCA1/2-deficient cells. Genes Dev. *35*, 1271–1289. https://doi.org/10.1101/gad.348479.121.

30. Schoonen, P.M., Talens, F., Stok, C., Gogola, E., Heijink, A.M., Bouwman, P., Foijer, F., Tarsounas, M., Blatter, S., Jonkers, J., et al. (2017). Progression through mitosis promotes PARP inhibitor-induced cytotoxicity in homologous recombination-deficient cancer cells. Nat. Commun. *8*, 15981. https://doi.org/10.1038/ncomms15981.

31. Feng, W., and Jasin, M. (2017). BRCA2 suppresses replication stress-induced mitotic and G1 abnormalities through homologous recombination. Nat. Commun. *8*, 525. https://doi.org/10.1038/s41467-017-00634-0.

32. Lai, X., Broderick, R., Bergoglio, V., Zimmer, J., Badie, S., Niedzwiedz, W., Hoffmann, J.S., and Tarsounas, M. (2017). MUS81 nuclease activity is essential for replication stress tolerance and chromosome segregation in BRCA2-deficient cells. Nat. Commun. *8*, 15983. https://doi.org/10.1038/ncomms15983.

33. Ter Brugge, P., Kristel, P., van der Burg, E., Boon, U., de Maaker, M., Lips, E., Mulder, L., de Ruiter, J., Moutinho, C., Gevensleben, H., et al. (2016). Mechanisms of Therapy Resistance in Patient-Derived Xenograft Models of BRCA1-Deficient Breast Cancer. J. Natl. Cancer Inst. *108*. https://doi.org/10.1093/jnci/djw148.

34. Lheureux, S., Bruce, J.P., Burnier, J.V., Karakasis, K., Shaw, P.A., Clarke, B.A., Yang, S.Y.C., Quevedo, R., Li, T., Dowar, M., et al. (2017). Somatic BRCA1/2 Recovery as a Resistance Mechanism After Exceptional Response to Poly (ADP-ribose) Polymerase Inhibition. J. Clin. Oncol. *35*, 1240–1249. https://doi.org/10.1200/JCO.2016.71.3677.

35. Pishvaian, M.J., Biankin, A.V., Bailey, P., Chang, D.K., Laheru, D., Wolfgang, C.L., and Brody, J.R. (2017). BRCA2 secondary mutation-mediated resistance to platinum and PARP inhibitor-based therapy in pancreatic cancer. Br. J. Cancer *116*, 1021–1026. https://doi.org/10.1038/bjc.2017.40.

36. Gornstein, E.L., Sandefur, S., Chung, J.H., Gay, L.M., Holmes, O., Erlich, R.L., Soman, S., Martin, L.K., Rose, A.V., Stephens, P.J., et al. (2018). BRCA2 Reversion Mutation Associated With Acquired Resistance to Olaparib in Estrogen Receptor-positive Breast Cancer Detected by Genomic Profiling of Tissue and Liquid Biopsy. Clin. Breast Cancer *18*, 184–188. https://doi.org/10.1016/j.clbc.2017.12.010.

37. Edwards, S.L., Brough, R., Lord, C.J., Natrajan, R., Vatcheva, R., Levine, D.A., Boyd, J., Reis-Filho, J.S., and Ashworth, A. (2008). Resistance to therapy caused by intragenic deletion in BRCA2. Nature *451*, 1111–1115. https://doi.org/10.1038/nature06548.

38. Barber, L.J., Sandhu, S., Chen, L., Campbell, J., Kozarewa, I., Fenwick, K., Assiotis, I., Rodrigues, D.N., Reis Filho, J.S., Moreno, V., et al. (2013). Secondary mutations in BRCA2 associated with clinical resistance to a PARP inhibitor. J. Pathol. *229*, 422–429. https://doi.org/10.1002/path.4140.

39. Kondrashova, O., Nguyen, M., Shield-Artin, K., Tinker, A.V., Teng, N.N.H., Harrell, M.I., Kuiper, M.J., Ho, G.Y., Barker, H., Jasin, M., et al. (2017). Secondary Somatic Mutations Restoring RAD51C and RAD51D Associated with Acquired Resistance to the PARP Inhibitor Rucaparib in High-Grade Ovarian Carcinoma. Cancer Discov. *7*, 984–998. https://doi.org/10.1158/2159-8290.CD-17-0419.

40. Pettitt, S.J., Krastev, D.B., Brandsma, I., Dréan, A., Song, F., Aleksandrov, R., Harrell, M.I., Menon, M., Brough, R., Campbell, J., et al. (2018). Genome-wide and high-density CRISPR-Cas9 screens identify point mutations in PARP1 causing PARP inhibitor resistance. Nat. Commun. *9*, 1849. https://doi.org/10.1038/s41467-018-03917-2.

41. Gogola, E., Duarte, A.A., de Ruiter, J.R., Wiegant, W.W., Schmid, J.A., de Bruijn, R., James, D.I., Guerrero Llobet, S., Vis, D.J., Annunziato, S., et al. (2018). Selective Loss of PARG Restores PARylation and Counteracts PARP Inhibitor-Mediated Synthetic Lethality. Cancer Cell *33*, 1078–1093.e12. https://doi.org/10.1016/j.ccell.2018.05.008.

42. Escribano-Diaz, C., Orthwein, A., Fradet-Turcotte, A., Xing, M., Young, J.T., Tkac, J., Cook, M.A., Rosebrock, A.P., Munro, M., Canny, M.D., et al. (2013). A cell cycle-dependent regulatory circuit composed of 53BP1-RIF1 and BRCA1-CtIP controls DNA repair pathway choice. Mol Cell *49*, 872–883. https://doi.org/10.1016/j.molcel.2013.01.001.

43. Gupta, R., Somyajit, K., Narita, T., Maskey, E., Stanlie, A., Kremer, M., Typas, D., Lammers, M., Mailand, N., Nussenzweig, A., et al. (2018). DNA Repair Network Analysis Reveals Shieldin as a Key Regulator of NHEJ and PARP Inhibitor Sensitivity. Cell *173*, 972–988.e23. https://doi.org/10.1016/j.cell.2018.03.050.

44. Noordermeer, S.M., Adam, S., Setiaputra, D., Barazas, M., Pettitt, S.J., Ling, A.K., Olivieri, M., Álvarez-Quilón, A., Moatti, N., Zimmermann, M., et al. (2018). The shieldin complex mediates 53BP1-dependent DNA repair. Nature *560*, 117–121. https://doi.org/10.1038/s41586-018-0340-7.

45. Ghezraoui, H., Oliveira, C., Becker, J.R., Bilham, K., Moralli, D., Anzilotti, C., Fischer, R., Deobagkar-Lele, M., Sanchiz-Calvo, M., Fueyo-Marcos, E., et al. (2018). 53BP1 cooperation with the REV7-shieldin complex underpins DNA structure-specific NHEJ. Nature *560*, 122–127. https://doi.org/10.1038/s41586-018-0362-1.

46. Dev, H., Chiang, T.W.W., Lescale, C., de Krijger, I., Martin, A.G., Pilger, D., Coates, J., Sczaniecka-Clift, M., Wei, W., Ostermaier, M., et al. (2018). Shieldin complex promotes DNA end-joining and counters homologous recombination in BRCA1-null cells. Nat. Cell Biol. *20*, 954–965. https://doi.org/10.1038/s41556-018-0140-1.

47. Boersma, V., Moatti, N., Segura-Bayona, S., Peuscher, M.H., van der Torre, J., Wevers, B.A., Orthwein, A., Durocher, D., and Jacobs, J.J.L. (2015). MAD2L2 controls DNA repair at telomeres and DNA breaks by inhibiting 5' end resection. Nature *521*, 537–540. https://doi.org/10.1038/nature14216.

48. Xu, G., Chapman, J.R., Brandsma, I., Yuan, J., Mistrik, M., Bouwman, P., Bartkova, J., Gogola, E., Warmerdam, D., Barazas, M., et al. (2015). REV7 counteracts DNA double-strand break resection and affects PARP inhibition. Nature *521*, 541–544. https://doi.org/10.1038/nature14328.

49. Bunting, S.F., Callén, E., Wong, N., Chen, H.T., Polato, F., Gunn, A., Bothmer, A., Feldhahn, N., Fernandez-Capetillo, O., Cao, L., et al. (2010). 53BP1 inhibits homologous recombination in Brca1-deficient cells by blocking resection of DNA breaks. Cell *141*, 243–254. https://doi.org/10.1016/j.cell.2010.03.012.

50. Bouwman, P., Aly, A., Escandell, J.M., Pieterse, M., Bartkova, J., van der Gulden, H., Hiddingh, S., Thanasoula, M., Kulkarni, A., Yang, Q., et al. (2010). 53BP1 loss rescues BRCA1 deficiency and is associated with triple-negative and BRCA-mutated breast cancers. Nat. Struct. Mol. Biol. *17*, 688–695. https://doi.org/10.1038/nsmb.1831.

51. Mirman, Z., Lottersberger, F., Takai, H., Kibe, T., Gong, Y., Takai, K., Bianchi, A., Zimmermann, M., Durocher, D., and de Lange, T. (2018). 53BP1-RIF1-shieldin counteracts DSB resection through CST- and Polα-dependent fill-in. Nature *560*, 112–116. https://doi.org/10.1038/s41586-018-0324-7.

52. Barazas, M., Annunziato, S., Pettitt, S.J., de Krijger, I., Ghezraoui, H., Roobol, S.J., Lutz, C., Frankum, J., Song, F.F., Brough, R., et al. (2018). The CST Complex Mediates End Protection at Double-Strand Breaks and Promotes PARP Inhibitor Sensitivity in BRCA1-Deficient Cells. Cell Rep. *23*, 2107–2118. https://doi.org/10.1016/j.celrep.2018.04.046.

53. Becker, J.R., Cuella-Martin, R., Barazas, M., Liu, R., Oliveira, C., Oliver, A.W., Bilham, K., Holt, A.B., Blackford, A.N., Heierhorst, J., et al. (2018). The ASCIZ-DYNLL1 axis promotes 53BP1-dependent non-homologous end joining and PARP inhibitor sensitivity. Nat. Commun. *9*, 5406. https://doi.org/10.1038/s41467-018-07855-x.

54. He, Y.J., Meghani, K., Caron, M.C., Yang, C., Ronato, D.A., Bian, J., Sharma, A., Moore, J., Niraj, J., Detappe, A., et al. (2018). DYNLL1 binds to MRE11 to limit DNA end resection in BRCA1-deficient cells. Nature *563*, 522–526. https://doi.org/10.1038/s41586-018-0670-5.

55. Rondinelli, B., Gogola, E., Yücel, H., Duarte, A.A., van de Ven, M., van der Sluijs, R., Konstantinopoulos, P.A., Jonkers, J., Ceccaldi, R., Rottenberg, S., and D'Andrea, A.D. (2017). EZH2 promotes degradation of stalled replication forks by recruiting MUS81 through histone H3 trimethylation. Nat. Cell Biol. *19*, 1371–1378. https://doi.org/10.1038/ncb3626.

56. Guillemette, S., Serra, R.W., Peng, M., Hayes, J.A., Konstantinopoulos, P.A., Green, M.R., and Cantor, S.B. (2015). Resistance to therapy in BRCA2 mutant cells due to loss of the nucleosome remodeling factor CHD4. Genes Dev. *29*, 489–494. https://doi.org/10.1101/gad.256214.114.

57. Ray Chaudhuri, A., Callen, E., Ding, X., Gogola, E., Duarte, A.A., Lee, J.E., Wong, N., Lafarga, V., Calvo, J.A., Panzarino, N.J., et al. (2016). Replication fork stability confers chemoresistance in BRCA-deficient cells. Nature *535*, 382–387. https://doi.org/10.1038/nature18325.

58. Taglialatela, A., Alvarez, S., Leuzzi, G., Sannino, V., Ranjha, L., Huang, J.W., Madubata, C., Anand, R., Levy, B., Rabadan, R., et al. (2017). Restoration of Replication Fork Stability in BRCA1- and BRCA2-Deficient Cells by Inactivation of SNF2-Family Fork Remodelers. Mol. Cell *68*, 414–430.e8. https://doi.org/10.1016/j.molcel.2017.09.036.

59. Ceccaldi, R., Liu, J.C., Amunugama, R., Hajdu, I., Primack, B., Petalcorin, M.I.R., O'Connor, K.W., Konstantinopoulos, P.A., Elledge, S.J., Boulton, S.J., et al. (2015). Homologous-recombination-deficient tumours are dependent on Polθ-mediated repair. Nature *518*, 258–262. https://doi.org/10.1038/nature14184.

60. Mateos-Gomez, P.A., Gong, F., Nair, N., Miller, K.M., Lazzerini-Denchi, E., and Sfeir, A. (2015). Mammalian polymerase theta promotes alternative NHEJ and suppresses recombination. Nature *518*, 254–257. https://doi.org/10.1038/nature14157.

61. Rottenberg, S., Jaspers, J.E., Kersbergen, A., van der Burg, E., Nygren, A.O.H., Zander, S.A.L., Derksen, P.W.B., de Bruin, M., Zevenhoven, J., Lau, A., et al. (2008). High sensitivity of BRCA1-deficient mammary tumors to the PARP inhibitor AZD2281 alone and in combination with platinum drugs. Proc. Natl. Acad. Sci. USA *105*, 17079–17084. https://doi.org/10.1073/pnas.0806092105.

62. Jaspers, J.E., Sol, W., Kersbergen, A., Schlicker, A., Guyader, C., Xu, G., Wessels, L., Borst, P., Jonkers, J., and Rottenberg, S. (2015). BRCA2-deficient sarcomatoid mammary tumors exhibit multidrug resistance. Cancer Res. *75*, 732–741. https://doi.org/10.1158/0008-5472.CAN-14-0839.

63. Niraj, J., Färkkilä, A., and D'Andrea, A.D. (2019). The Fanconi Anemia Pathway in Cancer. Annu. Rev. Cancer Biol. *3*, 457–478. https://doi.org/10.1146/annurev-cancerbio-030617-050422.

64. Luke-Glaser, S., Luke, B., Grossi, S., and Constantinou, A. (2010). FANCM regulates DNA chain elongation and is stabilized by S-phase checkpoint signalling. EMBO J. *29*, 795–805. https://doi.org/10.1038/emboj.2009.371.

65. Blackford, A.N., Schwab, R.A., Nieminuszczy, J., Deans, A.J., West, S.C., and Niedzwiedz, W. (2012). The DNA translocase activity of FANCM protects stalled replication forks. Hum. Mol. Genet. *21*, 2005–2016. https://doi.org/10.1093/hmg/dds013.

66. Schwab, R.A., Blackford, A.N., and Niedzwiedz, W. (2010). ATR activation and replication fork restart are defective in FANCM-deficient cells. EMBO J. *29*, 806–818. https://doi.org/10.1038/emboj.2009.385.

67. Collis, S.J., Ciccia, A., Deans, A.J., Horejsí, Z., Martin, J.S., Maslen, S.L., Skehel, J.M., Elledge, S.J., West, S.C., and Boulton, S.J. (2008). FANCM and FAAP24 function in ATR-mediated checkpoint signaling independently of the Fanconi anemia core complex. Mol. Cell *32*, 313–324. https://doi.org/10.1016/j.molcel.2008.10.014.

68. Wang, Y., Leung, J.W., Jiang, Y., Lowery, M.G., Do, H., Vasquez, K.M., Chen, J., Wang, W., and Li, L. (2013). FANCM and FAAP24 maintain genome stability via cooperative as well as unique functions. Mol. Cell *49*, 997–1009. https://doi.org/10.1016/j.molcel.2012.12.010.

69. Deans, A.J., and West, S.C. (2009). FANCM connects the genome instability disorders Bloom's Syndrome and Fanconi Anemia. Mol. Cell *36*, 943–953. https://doi.org/10.1016/j.molcel.2009.12.006.

70. Panday, A., Willis, N.A., Elango, R., Menghi, F., Duffey, E.E., Liu, E.T., and Scully, R. (2021). FANCM regulates repair pathway choice at stalled replication forks. Mol. Cell *81*, 2428–2444.e6. https://doi.org/10.1016/j.molcel.2021.03.044.

71. Huang, J., Liu, S., Bellani, M.A., Thazhathveetil, A.K., Ling, C., de Winter, J.P., Wang, Y., Wang, W., and Seidman, M.M. (2013). The DNA translocase FANCM/MHF promotes replication traverse of DNA interstrand crosslinks. Mol. Cell *52*, 434–446. https://doi.org/10.1016/j.molcel.2013.09.021.

72. Huang, J., Zhang, J., Bellani, M.A., Pokharel, D., Gichimu, J., James, R.C., Gali, H., Ling, C., Yan, Z., Xu, D., et al. (2019). Remodeling of Interstrand Crosslink Proximal Replisomes Is Dependent on ATR, FANCM, and FANCD2. Cell Rep. *27*, 1794–1808.e5. https://doi.org/10.1016/j.celrep.2019.04.032.

73. Silva, B., Pentz, R., Figueira, A.M., Arora, R., Lee, Y.W., Hodson, C., Wischnewski, H., Deans, A.J., and Azzalin, C.M. (2019). FANCM limits ALT activity by restricting telomeric replication stress induced by deregulated BLM and R-loops. Nat. Commun. *10*, 2253. https://doi.org/10.1038/s41467-019-10179-z.

74. Lu, R., O'Rourke, J.J., Sobinoff, A.P., Allen, J.A.M., Nelson, C.B., Tomlinson, C.G., Lee, M., Reddel, R.R., Deans, A.J., and Pickett, H.A. (2019). The FANCM-BLM-TOP3A-RMI complex suppresses alternative lengthening of telomeres (ALT). Nat. Commun. *10*, 2252. https://doi.org/10.1038/s41467-019-10180-6.

75. Pan, X., Drosopoulos, W.C., Sethi, L., Madireddy, A., Schildkraut, C.L., and Zhang, D. (2017). FANCM, BRCA1, and BLM cooperatively resolve the replication stress at the ALT telomeres. Proc. Natl. Acad. Sci. USA *114*, E5940–E5949. https://doi.org/10.1073/pnas.1708065114.

76. Stoepker, C., Faramarz, A., Rooimans, M.A., van Mil, S.E., Balk, J.A., Velleuer, E., Ameziane, N., Te Riele, H., and de Winter, J.P. (2015). DNA helicases FANCM and DDX11 are determinants of PARP inhibitor sensitivity. DNA Repair *26*, 54–64. https://doi.org/10.1016/j.dnarep.2014.12.003.

77. Figlioli, G., Bogliolo, M., Catucci, I., Caleca, L., Lasheras, S.V., Pujol, R., Kiiski, J.I., Muranen, T.A., Barnes, D.R., Dennis, J., et al. (2019). The FANCM:p.Arg658* truncating variant is associated with risk of triple-negative breast cancer. NPJ Breast Cancer *5*, 38. https://doi.org/10.1038/s41523-019-0127-5.

78. Natsume, T., Kiyomitsu, T., Saga, Y., and Kanemaki, M.T. (2016). Rapid Protein Depletion in Human Cells by Auxin-Inducible Degron Tagging with Short Homology Donors. Cell Rep. *15*, 210–218. https://doi.org/10.1016/j.celrep.2016.03.001.

79. Kong, N., and Chan, Y.W. (2023). Protocol for biallelic tagging of an endogenous gene using CRISPR-Cas9 in human cells. STAR Protoc. *4*, 102286. https://doi.org/10.1016/j.xpro.2023.102286.

80. Singh, T.R., Bakker, S.T., Agarwal, S., Jansen, M., Grassman, E., Godthelp, B.C., Ali, A.M., Du, C.H., Rooimans, M.A., Fan, Q., et al. (2009). Impaired FANCD2 monoubiquitination and hypersensitivity to camptothecin uniquely characterize Fanconi anemia complementation group M. Blood *114*, 174–180. https://doi.org/10.1182/blood-2009-02-207811.

81. Yan, Z., Delannoy, M., Ling, C., Daee, D., Osman, F., Muniandy, P.A., Shen, X., Oostra, A.B., Du, H., Steltenpool, J., et al. (2010). A histone-fold complex and FANCM form a conserved DNA-remodeling complex to maintain genome stability. Mol. Cell *37*, 865–878. https://doi.org/10.1016/j.molcel.2010.01.039.

82. Pierce, A.J., Johnson, R.D., Thompson, L.H., and Jasin, M. (1999). XRCC3 promotes homology-directed repair of DNA damage in mammalian cells. Genes Dev. *13*, 2633–2638. https://doi.org/10.1101/gad.13.20.2633.

83. Meroni, A., Wells, S.E., Fonseca, C., Ray Chaudhuri, A., Caldecott, K.W., and Vindigni, A. (2023). DNA Combing versus DNA Spreading and the Separation of Sister Chromatids. Preprint at bioRxiv. https://doi.org/10.1101/2023.05.02.539129.

84. Taglialatela, A., Leuzzi, G., Sannino, V., Cuella-Martin, R., Huang, J.W., Wu-Baer, F., Baer, R., Costanzo, V., and Ciccia, A. (2021). REV1-Polzeta maintains the viability of homologous recombination-deficient cancer cells through mutagenic repair of PRIMPOL-dependent ssDNA gaps. Mol Cell *81*, 4008–4025.e4007. https://doi.org/10.1016/j.molcel.2021.08.016.

85. Kang, Z., Fu, P., Alcivar, A.L., Fu, H., Redon, C., Foo, T.K., Zuo, Y., Ye, C., Baxley, R., Madireddy, A., et al. (2021). BRCA2 associates with MCM10 to suppress PRIMPOL-mediated repriming and single-stranded gap formation after DNA damage. Nat. Commun. *12*, 5966. https://doi.org/10.1038/s41467-021-26227-6.

86. Mouron, S., Rodriguez-Acebes, S., Martinez-Jimenez, M.I., Garcia-Gomez, S., Chocron, S., Blanco, L., and Mendez, J. (2013). Repriming of DNA synthesis at stalled replication forks by human PrimPol. Nat. Struct. Mol. Biol. *20*, 1383–1389. https://doi.org/10.1038/nsmb.2719.

87. Costanzo, V., Shechter, D., Lupardus, P.J., Cimprich, K.A., Gottesman, M., and Gautier, J. (2003). An ATR- and Cdc7-dependent DNA damage checkpoint that inhibits initiation of DNA replication. Mol. Cell *11*, 203–213. https://doi.org/10.1016/s1097-2765(02)00799-2.

88. Chan, Y.W., Fugger, K., and West, S.C. (2018). Unresolved recombination intermediates lead to ultra-fine anaphase bridges, chromosome breaks and aberrations. Nat. Cell Biol. *20*, 92–103. https://doi.org/10.1038/s41556-017-0011-1.

89. Tiwari, A., Addis Jones, O., and Chan, K.L. (2018). 53BP1 can limit sister-chromatid rupture and rearrangements driven by a distinct ultrafine DNA bridging-breakage process. Nat. Commun. *9*, 677. https://doi.org/10.1038/s41467-018-03098-y.

90. Tao, Y., Jin, C., Li, X., Qi, S., Chu, L., Niu, L., Yao, X., and Teng, M. (2012). The structure of the FANCM-MHF complex reveals physical features for functional assembly. Nat. Commun. *3*, 782. https://doi.org/10.1038/ncomms1779.

91. Singh, T.R., Saro, D., Ali, A.M., Zheng, X.F., Du, C.H., Killen, M.W., Sachpatzidis, A., Wahengbam, K., Pierce, A.J., Xiong, Y., et al. (2010). MHF1-MHF2, a histone-fold-containing protein complex, participates in the Fanconi anemia pathway via FANCM. Mol. Cell *37*, 879–886. https://doi.org/10.1016/j.molcel.2010.01.036.

92. Leung, W., Simoneau, A., Saxena, S., Jackson, J., Patel, P.S., Limbu, M., Vindigni, A., and Zou, L. (2023). ATR protects ongoing and newly assembled DNA replication forks through distinct mechanisms. Cell Rep. *42*, 112792. https://doi.org/10.1016/j.celrep.2023.112792.

93. Wang, H., Li, S., Oaks, J., Ren, J., Li, L., and Wu, X. (2018). The concerted roles of FANCM and Rad52 in the protection of common fragile sites. Nat. Commun. *9*, 2791. https://doi.org/10.1038/s41467-018-05066-y.

94. Lossaint, G., Larroque, M., Ribeyre, C., Bec, N., Larroque, C., Décaillet, C., Gari, K., and Constantinou, A. (2013). FANCD2 binds MCM proteins and controls replisome function upon activation of s phase checkpoint signaling. Mol. Cell *51*, 678–690. https://doi.org/10.1016/j.molcel.2013.07.023.

95. Zhang, J., Bellani, M.A., James, R.C., Pokharel, D., Zhang, Y., Reynolds, J.J., McNee, G.S., Jackson, A.P., Stewart, G.S., and Seidman, M.M. (2020). DONSON and FANCM associate with different replisomes distinguished by replication timing and chromatin domain. Nat. Commun. *11*, 3951. https://doi.org/10.1038/s41467-020-17449-1.

96. Toledo, L.I., Altmeyer, M., Rask, M.B., Lukas, C., Larsen, D.H., Povlsen, L.K., Bekker-Jensen, S., Mailand, N., Bartek, J., and Lukas, J. (2013). ATR prohibits replication catastrophe by preventing global exhaustion of RPA. Cell *155*, 1088–1103. https://doi.org/10.1016/j.cell.2013.10.043.

97. Catucci, I., Osorio, A., Arver, B., Neidhardt, G., Bogliolo, M., Zanardi, F., Riboni, M., Minardi, S., Pujol, R., Azzollini, J., et al. (2018). Individuals with FANCM biallelic mutations do not develop Fanconi anemia, but show risk for breast cancer, chemotherapy toxicity and may display chromosome fragility. Genet. Med. *20*, 452–457. https://doi.org/10.1038/gim.2017.123.

98. Bogliolo, M., Bluteau, D., Lespinasse, J., Pujol, R., Vasquez, N., d'Enghien, C.D., Stoppa-Lyonnet, D., Leblanc, T., Soulier, J., and Surrallés, J. (2018). Biallelic truncating FANCM mutations cause early-onset cancer but not Fanconi anemia. Genet. Med. *20*, 458–463. https://doi.org/10.1038/gim.2017.124.

99. Kong, N., Liu, Z., and Chan, Y.W. (2023). RIF1 suppresses the formation of single-stranded ultrafine anaphase bridges via protein phosphatase 1. Cell Rep. *42*, 112032. https://doi.org/10.1016/j.celrep.2023.112032.

100. Ran, F.A., Hsu, P.D., Wright, J., Agarwala, V., Scott, D.A., and Zhang, F. (2013). Genome engineering using the CRISPR-Cas9 system. Nat. Protoc. *8*, 2281–2308. https://doi.org/10.1038/nprot.2013.143.

101. Xue, Y., Li, Y., Guo, R., Ling, C., and Wang, W. (2008). FANCM of the Fanconi anemia core complex is required for both monoubiquitination and DNA repair. Hum. Mol. Genet. *17*, 1641–1652. https://doi.org/10.1093/hmg/ddn054.

102. Zou, J., Zhang, D., Qin, G., Chen, X., Wang, H., and Zhang, D. (2014). BRCA1 and FancJ cooperatively promote interstrand crosslinker induced centrosome amplification through the activation of polo-like kinase 1. Cell Cycle *13*, 3685–3697. https://doi.org/10.4161/15384101.2014.964973.

103. Schindelin, J., Arganda-Carreras, I., Frise, E., Kaynig, V., Longair, M., Pietzsch, T., Preibisch, S., Rueden, C., Saalfeld, S., Schmid, B., et al. (2012). Fiji: an open-source platform for biological-image analysis. Nat. Methods *9*, 676–682. https://doi.org/10.1038/nmeth.2019.

STAR★METHODS

KEY RESOURCES TABLE

REAGENT or RESOURCE	SOURCE	IDENTIFIER
Antibodies		
Mouse monoclonal anti-FANCM	gift from Stephen West	N/A
Rabbit polyclonal anti-OsTIR1	MBL	Cat# PD048; RRID: AB_2909494
Rabbit polyclonal anti-53BP1	Abcam	Cat# ab36823; RRID: AB_722497
Rabbit polyclonal anti-PARP1	Cell Signaling	Cat# 9542; RRID: AB_2160739
Mouse monoclonal anti-RPA2 (9H8)	Abcam	Cat# ab2175; RRID: AB_302873
Rabbit polyclonal anti- RPA2 pSer4/8	Bethyl	Cat# A300-245A; RRID: AB_210547
Mouse monoclonal anti-α-tubulin	Sigma-Aldrich	Cat# 00020911; RRID: AB_10013740
Mouse monoclonal anti-vinculin(7F9)	Santa Cruz	Cat# sc-73614; RRID: AB_1131294
Rabbit polyclonal anti-Histone H3	Abcam	Cat# ab1791; RRID: AB_302613
Mouse polyclonal anti-CHK1	Sigma-Aldrich	Cat# C9358; RRID: AB_259159
Rabbit polyclonal anti-CHK1 pSer317	Cell Signaling	Cat# 2344; RRID: AB_331488
Mouse monoclonal anti-CHK2	Millipore	Cat# 05–649; RRID: AB_2244941
Rabbit polyclonal anti-CHK2 pThr68	Cell Signaling	Cat# 2661; RRID: AB_331479
Rabbit polyclonal anti-FANCD2	Novus	Cat# NB100-182; RRID: AB_10002867
Mouse monoclonal anti-ATM pSer1981	Millipore	Cat# 05–740; RRID: AB_309954
Human anti-centromere	Immunovision	Cat# HCT-0100; RRID: AB_2744669
Rat polyclonal anti-BrdU	Abcam	Cat#ab6326; RRID: AB_305426
Mouse monoclonal anti-BrdU	BD Biosciences	Cat#347580; RRID: AB_400326
Rabbit polyclonal anti-PRIMPOL	Proteintech	Cat#29824-1-AP; RRID: AB_2918349
Alexa Fluor 488 F(ab')2-goat anti-rabbit IgG	Thermo Fisher	Cat# A-11070; RRID: AB_2534114
Alexa Fluor 546 goat anti-rabbit IgG	Thermo Fisher	Cat# A11010; RRID: AB_2534077
Alexa Fluor 488 goat anti-mouse IgG	Thermo Fisher	Cat# A27034; RRID: AB_2536097
Alexa Fluor 555 goat anti-mouse IgG	Thermo Fisher	Cat# A28180; RRID: AB_2536164
Alexa Fluor 555 goat anti-rat IgG	Thermo Fisher	Cat# A-21434; RRID: AB_141733
Goat anti-rabbit IgG-HRP conjugate	Bio-Rad	Cat# 1706515; RRID: AB_11125142
Goat anti-mouse IgG-HRP conjugate	Bio-Rad	Cat# 1706516; RRID: AB_11125547
Chemicals, peptides, and recombinant proteins		
DMEM, powder, high glucose, pyruvate	Thermo Fisher	Cat# 12800082
Penicillin-Streptomycin (10,000 U/mL)	Thermo Fisher	Cat# 15140122
Trypsin-EDTA (0.25%), phenol red	Thermo Fisher	Cat# 25200072
Pierce™ 16% Formaldehyde (w/v), Methanol-free	Thermo Fisher	Cat# 28908
ProLong™ Diamond Antifade Mountant	Thermo Fisher	Cat# P36961
Alexa Fluor 647 Azide, Triethylammonium Salt	Thermo Fisher	Cat# A10277
Alexa Fluor 488 Azide, Triethylammonium Salt	Thermo Fisher	Cat# A10266
RNase A	Thermo Fisher	Cat# 12091021
Propodium iodide	Sigma-Aldrich	Cat# P4864
Dox: Doxycycline hyclate	Sigma-Aldrich	Cat# D9891
IAA: 3-Indoleacetic acid	Sigma-Aldrich	Cat# I2886
ICRF-193	Sigma-Aldrich	Cat# I4659
RO-3306	Cayman	Cat# 15149
Cisplatin	Cayman	Cat# 13119
Camptothecin	Cayman	Cat# 11694
Lipofectamine RNAiMAX Reagent	Thermo Fisher	Cat# 13778-150
Lipofectamine 2000	Thermo Fisher	Cat# 11668-019

(*Continued on next page*)

Continued

REAGENT or RESOURCE	SOURCE	IDENTIFIER
Zeocin	Thermo Fisher	Cat# R25001
Puromycin	Thermo Fisher	Cat# A11138-02
Geneticin	Thermo Fisher	Cat# 10131035
SuperSignal West Pico PLUS Chemiluminescent Substrate	Thermo Fisher	Cat# 34580
Colcemid	Thermo Fisher	Cat# 15212012
Insulin, human recombinant	Thermo Fisher	Cat# 12585014
Hydrocortisone	Sigma-Aldrich	Cat# H4001
5-Chloro-2′-deoxyuridine thymidine analog, CldU	Sigma-Aldrich	Cat# C6891
5-Iodo-2 -deoxyuridine, IdU	Sigma-Aldrich	Cat# 17125
Nocodazole	Sigma-Aldrich	Cat# M1404
5-Ethynyl-2′-deoxyuridine, EdU	Cayman	Cat# 20518
Etoposide	Sigma-Aldrich	Cat# 341205
Olaparib	Cayman	Cat# 10621
Veliparib	Cayman	Cat# 11505
Methyl methanesulfonate	Sigma-Aldrich	Cat# 129925
Hydroxyurea	Sigma-Aldrich	Cat# H8627
S1 Nuclease	Thermo Fisher	Cat# EN0321
Protease and Phosphatase Inhibitor	Thermo Fisher	Cat# A32961
Protease Inhibitor Tablets	Thermo Fisher	Cat# A32965
Q5 High-Fidelity DNA polymerase	New England Biolabs	Cat#M0491S
Critical commercial assays		
NucleoSpin Plasmid Transfection-grade, Mini kit	Macherey-Nagel	Cat# 740490.250
NucleoBond Xtra Midi kit, transfection-grade	Macherey-Nagel	Cat# 740410.50
GeneJET Gel Extraction Kit	Thermo Fisher	Cat# K0691
DNA Ligation Kit, Mighty Mix	TaKaRa	Cat# 6023
CloneJET PCR Cloning Kit	Thermo Fisher	Cat# K1231
Subcellular Protein Fractionation Kit for Cultured Cells	Thermo Fisher	Cat# 78840
Experimental models: Cell lines		
HCT116	ATCC	Cat# CCL-247
HCT116: OsTIR1	Previous study[99]	N/A
HCT116: OsTIR1 FANCM-mAID-GFP	This paper	N/A
HCT116: OsTIR1 FANCM-mAID-GFP 53BP1 KO	This paper	N/A
HCT116: OsTIR1 FANCM-mAID-GFP PARP1 KO	This paper	N/A
293 DR-GFP	gift from Stephen West	N/A
MCF-7	ATCC	Cat# HTB-22
SUM149PT	gift from Stephen West	N/A
Oligonucleotides		
See Table S1	N/A	N/A
Recombinant DNA		
Plasmid: pMK289 (mAID-mClover-NeoR)	Addgene	Cat# 72827
Plasmid: pMK289 (mAID-mClover-BleoR)	Previous study[99]	N/A
Plasmid: pMK243 (Tet-OsTIR1-PURO)	Addgene	Cat# 72835
Plasmid: pX330-U6-Chimeric_BB-cBh-hSpCas9	Addgene	Cat# 42230
Plasmid: pX330-sgPRIMPOL	This paper	N/A
Plasmid: pMA-RQ FANCM	This paper	N/A
Plasmid: pMA-RQ FANCM-mAID-Clover (Zeo)	This paper	N/A
Plasmid: pMA-RQ FANCM-mAID-Clover (*Neo*)	This paper	N/A
Plasmid: pX330 sgFANCM C terminus	This paper	N/A
Plasmid: pSpCas9(BB)-2A-Puro (PX459) V2.0	Addgene	Cat# 62988

(*Continued on next page*)

Continued

REAGENT or RESOURCE	SOURCE	IDENTIFIER
Plasmid: PX459 V2.0-sg53BP1	This paper	N/A
Plasmid: PX459 V2.0-sgPARP1	This paper	N/A
Plasmid: pCBASce	Addgene	Cat #26477
Software and algorithms		
FIJI	Open Source	https://imagej.net/software/fiji/
Prism 10	GraphPad	https://www.graphpad.com
Adobe Photoshop	Adobe	https://www.adobe.com/
SoftWoRx	Cytiva Life Sciences	https://www.cytivalifesciences.com/
CellProfiler ver. 4.2.6	Broad Institute	https://cellprofiler.org

RESOURCE AVAILABILITY

Lead contact

Further information and requests for resources and reagents should be directed to and will be fulfilled by the lead contact, Ying Wai Chan (gywchan@hku.hk).

Materials availability

All reagents generated in this study are available from the lead contact upon request without restrictions.

Data and code availability

- All data reported in this paper will be shared by the lead contact upon request.
- This paper does not report original code.
- Any additional information required to reanalyze the data reported in this work paper is available from the lead contact upon request.

EXPERIMENTAL MODEL AND STUDY PARTICIPANT DETAILS

HCT116 and MCF-7 cells were obtained from the American Type Culture Collection (ATCC). SUM149PT and 293 DR-GFP cells were gifts from Stephen West (The Francis Crick Institute). HCT116, MCF-7 and 293 cells were cultured in Dulbecco's Modified Eagle Medium (DMEM), supplemented with 10% fetal bovine serum (Thermo Fisher) and 1% penicillin-streptomycin (100 U/mL, Thermo Fisher) in a 37°C incubator with 5% CO_2. SUM149PT cells were cultured in F-12 Hams (Thermo Fisher) supplemented with 5% FBS, insulin (5 μg/mL, Thermo Fisher), hydrocortisone (1 μg/mL, Sigma-Aldrich) and penicillin/streptomycin (100 U/mL, Thermo Fisher). The antibiotics used for selection of stable clones, puromycin (1 μg/mL), geneticin (500 μg/mL) and zeocin (50 μg/mL), were obtained from Thermo Fisher (key resources table).

METHOD DETAILS

Plasmid construction

To construct CRISPR-Cas9 plasmid expressing sgRNA targeting the last exon of FANCM, a pair of annealed oligonucleotides (target sequence: ATAATCAAGCTGCTCAAGAT) was cloned into pX330 plasmid (Addgene #42230) according to the published protocol.[100] Donor plasmids pMA-RQ-FANCM-mAID-Clover (Zeo) and pMA-RQ-FANCM-mAID-Clover (*Neo*) for endogenous tagging of FANCM with mAID-Clover tag were based on pMK289 (Addgene #72827) and pMK289-BleoR,[99] as previously described.[78] In brief, pMA-RQ-FANCM with ~500-bp homology arms and a BamHI site in between the homology arms was synthesized from gene synthesis (Thermo Fisher). The fragment of mAID-Clover-Neo/Zeo was cut out from pMK289 or pMK289-BleoR by BamHI and cloned into pMA-RQ-FANCM.

PARP1 sgRNA, 53BP1 sgRNA and PRIMPOL sgRNA were cloned in pX330 or pX459 v2.0 (Addgene # 62988) (target sequence of PARP1: TGGGTTCTCTGAGCTTCGGT; target sequence of 53BP1: CTGCTCAATGACCTGACTGA; target sequence of PRIMPOL: GATAGCGCTCCAGAGACAAC). All oligonucleotides were obtained from IDT (key resources table).

Transfection and cell line generation

To generate $HCT116^{FANCM\text{-}mAID\text{-}GFP}$ cell line, $HCT116^{TIR1}$ cells[99] were transfected with pX330 sgFANCM and the two donor plasmids with Lipofectamine 2000 (Thermo Fisher), followed by selection with geneticin (500 μg/mL) and zeocin (50 μg/mL). To induce

degradation of tagged FANCM protein, cells were treated with Dox (1 μg/mL) and indole-3-acetic acid (IAA, 250 μM). Isolated clones were verified by western blotting for FANCM degradation and biallelic tagging of FANCM was confirmed by genomic PCR.

To generate 53BP1, PARP1 and PRIMPOL knockout in HCT116$^{FANCM\text{-}mAID\text{-}GFP}$ cells, cells were transfected with the sgRNA-expressing plasmids using Lipofectamine 2000, followed by single clone isolation and verification by western blotting.

RNA interference

Cells were transfected with the following siRNAs (20 nM) using Lipofectamine RNAiMAX (Thermo Fisher) according to the manufacturer's instructions: control siRNA, FANCM siRNAs,[101] or BRCA1 siRNA.[102] See key resources table for their sequences. SMARTPool FANCB siRNAs (M-016941-01-0005) were purchased from Dharmacon.

Genomic PCR

To prepare genomic DNA, cells were harvested, and genomic DNA was extracted by DNeasy Blood & Tissue Kit (Qiagen) according to the manufacturer's instructions. PCR was carried out to confirm the biallelic tagging of *FANCM* using Q5 High-Fidelity 2X Master Mix (New England Biolabs) with primers p1, p2 and p3 (key resources table).

Antibodies

Primary antibodies (host animal, identification clone, supplier name and dilution with applications) used in this study are as follows: anti-FANCM (mouse; raised against FANCM$^{1507\text{-}1679}$, a gift from Stephen West; 1:1000 for WB), anti-OsTIR1 (rabbit; PD048; MBL; 1:1000 for WB), anti-FANCD2 (mouse; sc-20020; Santa Cruz; 1:100 for WB), anti-53BP1 (rabbit; EPR2172(2); Abcam; 1:1000 for IF), anti-RPA2 (mouse; 9H8; Abcam; 1:1000 for WB and IF), anti-RPA2 pSer4/pSer8 (rabbit; A300-245A; Bethyl; 1:1000 for WB and IF), anti-α-tubulin (mouse; TAT-1; Sigma-Aldrich; 1:5000 for WB), anti-Histone H3 (rabbit; EPR16987; Abcam; 1:2000 for WB), anti-ATM pSer1981 (mouse; 05–740; Millipore; 1:1000 for IF), anti-CHK1 (mouse; DCS-310; Sigma-Aldrich; 1:1000 for WB), anti-CHK1 pSer317 (rabbit; 2344; Cell Signaling; 1:1000 for WB), anti-CHK2 (mouse; 05–649 Millipore; 1:1000 for WB), anti-CHK2 pThr68 (rabbit; 2661; Cell Signaling; 1:1000 for WB), anti-PARP1 (rabbit, 9542, Cell Signaling; 1:1000 for WB), anti-BRCA1 (rabbit; 07–434; Millipore; 1:500 for IF), anti-PRIMPOL (rabbit; 29824-1-AP; Proteintech; 1:1000 for WB). Secondary antibodies (key resources table) were used at 1:2000 dilution for western blotting and immunofluorescence.

Protein extraction and western blotting

To prepare whole cell protein lysates, cells were collected and then lysed for 30 min in Tris-lysis buffer (50 mM Tris pH 7.5, 150 mM NaCl, 1% Triton X-100, 1 mM EDTA, 1 mM DTT) supplemented with protease inhibitors and phosphatase inhibitor cocktail (Thermo Fisher). The lysates were incubated on ice for 30 min, and then centrifugation (13,500 rpm for 30 min at 4°C). Protein concentrations were determined using Bradford Assay (Biorad) and equal amounts of total proteins were loaded in each lane of the SDS-PAGE. To prepare a subcellular fraction of nuclear soluble and chromatin-bound fraction, we used a subcellular protein fractionation kit from Thermo Fisher (78840) following the manufacturer's instructions. Proteins were transferred to nitrocellulose membranes using wet transfer method. Membranes were sequentially incubated with primary and secondary antibodies (key resources table). Proteins were detected by SuperSignal West Pico PLUS Chemiluminescent Substrate (Thermo Fisher) and the UVITEC Alliance Q9 Mini imaging system.

Flow cytometry

Cells were fixed with 70% ice-cold ethanol for 30 min. Fixed cells were washed twice with PBS and incubated with 50 μL of RNase A (100 μg/mL) and 400 μL of propidium iodide (50 μg/mL) for 30 min. The cell solution was cleaned by a fine mesh filter and then analyzed by a FACSAria III Cell Sorter (BD Biosciences). At least 10,000 cells were acquired per sample. Cell doublets and debris were excluded from the analyses. For EdU-pulse chase, cells were treated with EdU (10 μM) for 30 min before treated with olaparib for different time points. Cells were fixed with 70% ice-cold ethanol for 30 min. Fixed cells were then washed with PBS and PBS-T (PBS with 1% BSA and 0.1% Tween 20). Cells were incubated with 0.5 mL Click-iT reaction buffer (440 μL PBS, 10 μL of 100 mM copper sulfate, 0.5 μL Alexa Flour 647 azide (Thermo Fisher) and 50 μL 1M asorbic acid) for 30 min. After washed in PBS-T twice, cells were resuspended in 400 μL of propidium iodide solution with RNase A for 30 min and analyzed by FACSAria III Cell Sorter.

Immunofluorescence and microscopy

For immunofluorescence analyses, cells were cultured on coverslips and fixed in PTEMF buffer (20 mM PIPES pH 6.8, 0.2% Triton X-100, 1 mM $MgCl_2$, 10 mM EGTA and 4% paraformaldehyde) for 10 min. Fixed cells were permeabilized with 0.2% Triton X-100 in PBS for 10 min, followed by blocking with 3% BSA in PBS for 30 min. To fluorescently label EdU to identify S phase cells, cells were incubated with EdU (10 μM) for 30 min prior to fixation. The Click-iT reaction using Alexa Flour 488 azide (Thermo Fisher) was performed before antibody staining. Subsequently, Cells were incubated with diluted primary antibodies for 1.5 h. The coverslips were then washed with PBS and incubated with diluted secondary antibodies for 1.5 h. DNA was stained with DAPI (0.5 μg/mL). Coverslips were mounted on microscope slides with Prolong Diamond antifade mountant (Thermo Fisher). Images were acquired either using a Nikon Ti60 microscope equipped with DS-Ri2 camera under 40x air objective or 100x oil immersion objective, or DeltaVision Ultra microscope (Cytiva Life Sciences) equipped with PlanApo 60x/1.50 oil immersion objective (Olympus) and a CoolSNAP HQ camera

(Photometrics). Images taken from the DeltaVision microscope at single focal planes were processed with a deconvolution algorithm, and optical sections were projected into one picture using Softworx software (Cytiva Life Sciences). Acquired images were processed using Adobe Photoshop. Quantifications of foci number and intensity were done using CellProfiler ver. 4.2.6 (Broad Institute).

Clonogenic cell survival and cell variability assays

For clonogenic assay, 200 cells were seeded in each well of 6-well plates and treated with or without Dox and IAA. One day later, cells were treated with the indicated concentrations of cisplatin, camptothecin or methyl methanesulfonate for 1 day, olaparib, veliparib, etoposide or hydroxyurea for 7 days. Medium was replaced every 4 days. After 10 days, cells were fixed with ice-cold methanol for 5 min and stained with 40 mg/mL crystal violet solution (Sigma-Aldrich) containing 20% ethanol for 5 min. The percentage of cell survival was calculated against the untreated condition. For cell variability assay, 500–800 cells transfected with siRNAs were seeded in each well of 96-well plates. One day later, Cells were treated with the indicated concentrations of olaparib for 7 or 10 days. Cell variability was determined using cell counting kit 8 (Abcam) and the absorbance was measured at 460 nm using a plate reader.

Metaphase spread

Cells were treated with olaparib (500 nM) for 72 h, and then arrested in mitosis by treatment of colcemid (0.2 μg/mL) for 1.5 h before being harvested. Cells were washed one time with PBS and incubated with pre-warmed 75 mM KCl for 15 min at 37°C. Cells were resuspended with freshly prepared fixative solution (1:3 acetic acid: methanol) for 20 min. After repeating the fixation three times, pellets were resuspended in 0.3–0.5 mL fixative solution. 100–150 μL cell suspension was spread onto a pre-washed microscope slide from a ∼30–50 cm height. Slides were thoroughly air-dried and stained using Giemsa solution (7% Giemsa in 10 mM PIPES, pH 6.8). Images were acquired using a Nikon Ti60 microscope equipped with DS-Ri2 camera under a 100x oil immersion objective.

SMART assay

Cells were treated with 10 μM IdU for 24 h, followed by olaparib (10 μM, 24 h) or CPT (1 μM, 2 h). Cell pellets were washed with ice-cold PBS twice and resuspended with the ice-cold PBS at 200–400 cells/μl. Cells were mixed with IdU-unlabeled cells at the same concentration in a 1:5 proportion. DNA spreads were prepared by spotting 2.5 μL of cells on a SuperFrost Plus slide (Thermo Fisher), allowed to air-dry for 5–7 min and followed by lysis with 8 μL of spreading buffer (200 mM Tris-HCl pH 7.4, 50 mM EDTA, 0.5% SDS). Slides were tilted at 40° to horizontal, allowing DNA to run slowly down the slide at a constant speed. The droplet should reach the bottom edge after 3 to 5 min. The slides were air-dried and then fixed in methanol/acetic acid (3:1) at −20°C for 15 min. Slides were washed in PBS twice and then incubated in 70% ethanol and 30% water overnight at 4°C. Slides were washed in PBS twice and blocked in 3% BSA in PBS for 1 h. Slides were subsequently incubated with mouse anti-bromodeoxyuridine (BrdU) antibody (B44, Becton Dickinson, 1:100 dilution in blocking solution) for 1 h at 37°C. The slides were then washed with PBS and incubated with anti-mouse IgG Alexa Fluor 488 (1:100 dilution in blocking solution) for 1.5 h at 25°C. Slides were washed 3 times for 5 min with PBS, and mounted with ProLong Gold Antifade mountant (Thermo Fisher). Images were acquired using a Nikon Ti60 microscope equipped with a DS-Ri2 camera under a 100x oil immersion objective. Fiber length was measured using Fiji software.[103]

Native BrdU staining

Cells were seeded on coverslips and treated with 20 μM BrdU for 48 h, followed by olaparib (10 μM, 24h) or CPT (1 μM, 2 h). Cells were washed with ice-cold PBS one time and added ice-cold pre-extraction buffer (25mM HEPES pH 7.5, 50mM NaCl, 1mM EDTA, 3mM MgCl2, 300mM Sucrose, 0.5% Triton X-100) for 5 min over ice. Cells were fixed in ice-cold 4% paraformaldehyde for 10 min at 25°C, followed by blocking with 3% BSA in PBS for 30 min. Cells were subsequently incubated with mouse anti-BrdU antibody (1:100 dilution in blocking solution) for 1 h at 37°C, washed 3 times for 5 min with PBS. The slides were then incubated with anti-mouse IgG Alexa Fluor 488 (1:100 dilution in blocking solution) for 1.5 h at 25°C. Slides were then washed 3 times for 5 min with PBS.DNA was stained with DAPI (0.5 μg/mL) for 5 min. Coverslips were mounted on microscope slides with Prolong Diamond antifade mountant (Thermo Fisher). Images were acquired using a Nikon Ti60 microscope equipped with DS-Ri2 camera under 40x air objective. Quantifications of foci number and intensity were done using CellProfiler ver. 4.2.6 (Broad Institute).

DNA fiber analysis with S1 nuclease treatment

Cells were treated with 25 mM IdU and incubated for 20 min. Cells were washed two times with medium and then treated with 250 mM CldU for 60 min. Cells were permeabilized with CSK100 buffer (100 mM NaCl, 10 mM HEPES pH 7.0, 3 mM $MgCl_2$, 300 mM sucrose, 0.5% Triton X-100, pH 7.0) for 7 min at room temperature, washed once with cold PBS, once with S1 nuclease buffer (30 mM sodium acetate pH 4.6, 10 mM zinc acetate, 5% glycerol, 50 mM NaCl), and incubated with or without 20 U/mL S1 nuclease (Thermo Fisher) in S1 nuclease buffer for 1 h at 37°C. After the removal of the S1 nuclease buffer, PBS with 0.1% BSA was added. Nuclei were then scraped and centrifuged at 7000 rpm for 5 min at 4°C. The supernatant was then removed, leaving an appropriate volume to obtain 400-800 nuclei/μL. Nuclei were then resuspended, and DNA spreads were prepared by spotting 2 μL of cells on a SuperFrost Plus slide (Thermo Fisher), allowed to air-dry for 5–7 min and followed by lysis with 8 μL of spreading buffer (200 mM Tris-HCl pH 7.4, 50 mM EDTA, 0.5% SDS). Slides were tilted at 40° to horizontal, allowing DNA to run slowly down the slide at a constant speed. The droplet should reach the bottom edge after 3 to 5 min. The slides were air-dried and then fixed in methanol/acetic acid (3:1) for 10 min at 25°C. Slides were then washed 3 times for 5 min with water. DNA was denatured by 2.5 M HCl for

60 min at 25°C, followed by washing with PBS and blocking solution (3% BSA in PBS). Slides were blocked for 1 h in blocking solution and subsequently incubated with rat anti-BrdU (detects CldU, Abcam, ab6326, 1:100 dilution in blocking solution) and mouse anti-BrdU (detects IdU, B44, Becton Dickinson, 1:100 dilution in blocking solution) for 1.5 h, washed 3 times for 5 min with PBS with 0.1% Tween 20. The slides were then incubated with anti-rat IgG Alexa Fluor 555 and anti-mouse IgG Alexa Fluor 488 (both at 1:100 dilution in blocking solution) for 1.5 h. Slides were then washed 3 times for 5 min with PBS with 0.1% Tween 20. Slides were mounted with ProLong Gold Antifade mountant (Thermo Fisher). Images were acquired using a Nikon Ti60 microscope equipped with a DS-Ri2 camera under a 100x oil immersion objective. The length of fibers was measured using Fiji software.[103]

QUANTIFICATION AND STATISTICAL ANALYSIS

Custom CellProfiler pipelines based on the ''speckle'' template were used for automatic detection of DNA damage foci. Statistical significances were calculated using the unpaired two-tailed t test. A p value of 0.05 was considered borderline for statistical significance. *$p < 0.05$, **$p < 0.01$, ***$p < 0.001$ and ****$p < 0.0001$. Error bars represent mean ± standard deviation (SD) between the experiments. In Figure legends, n represents the number of independent experiments. Graphs were generated using GraphPad Prism 10. Sample size, number of independent experiments, and p values are indicated in the figures and figure legends.